REVIEW ARTICLE

Laser-induced optothermal response of gold nanoparticles: From a physical viewpoint to cancer treatment application

Somayeh Asadi[1]* [ORCID] | **Leonardo Bianchi[1]** | **Martina De Landro[1]** |
Sanzhar Korganbayev[1] | **Emiliano Schena[2]** | **Paola Saccomandi[1]**

[1]Department of Mechanical Engineering, Politecnico di Milano, Milan, Italy

[2]Laboratory of Measurement and Biomedical Instrumentation, Università Campus Bio-Medico di Roma, Rome, Italy

*Correspondence
Somayeh Asadi, Department of Mechanical Engineering, Politecnico di Milano, Milan 20156, Italy.
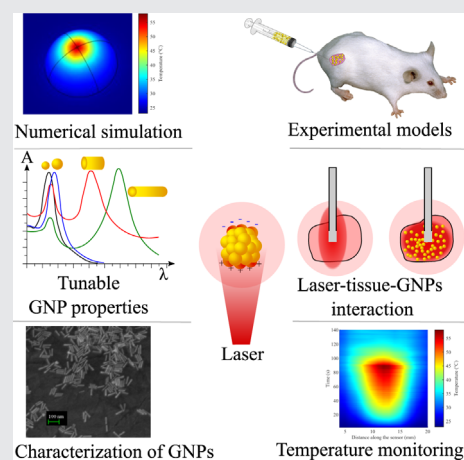Email: somayeh.asadi@polimi.it

Funding information
European Research Council (ERC) under the European Union's Horizon 2020 Research and Innovation Program, Grant/Award Number: 759159

Abstract

Gold nanoparticles (GNPs)-based photothermal therapy (PTT) is a promising minimally invasive thermal therapy for the treatment of focal malignancies. Although GNPs-based PTT has been known for over two decades and GNPs possess unique properties as therapeutic agents, the delivery of a safe and effective therapy is still an open question. This review aims at providing relevant and recent information on the usage of GNPs in combination with the laser to treat cancers, pointing out the practical aspects that bear on the therapy outcome. Emphasis is given to the assessment of the GNPs' properties and the physical mechanisms underlying the laser-induced heat generation in GNPs-loaded tissues. The main techniques available for temperature measurement and the current theoretical simulation approaches predicting the therapeutic outcome are reviewed. Topical challenges in delivering safe thermal dosage are also presented with the aim to discuss the state-of-the-art and the future perspective in the field of GNPs-mediated PTT.

KEYWORDS

gold nanoparticles, laser, near-infrared, photothermal therapy, simulation

Numerical simulation | Experimental models

Tunable GNP properties | Laser | Laser-tissue-GNPs interaction

Characterization of GNPs | Temperature monitoring

1 | INTRODUCTION

The development of novel and effective cancer treatment strategies has always been among the main missions of the biomedical community all over the world. Different treatment modalities are available to treat cancers and are used either alone or in combination with other

methods. Among several approaches, thermal therapy is being proposed as an alternative to traditional resection surgery for tumor removal, thanks to the possibility to be delivered in a minimally invasive manner, allowing several advantages, such as less pain and shorter recovery time [1,2]. The range of temperature between 43°C and 60°C, with specific exposure time, is responsible, at different levels, for the tumor thermal damage, due to proteins denaturation, microvasculature collapse, DNA impair apoptosis and necrosis [3]. Although there are differences in optical properties between the cancerous cells and healthy tissue (different reactions to radiation), the overall thermal effect in the tumor and the surrounding healthy cells does not present appreciable selectivity, once exposed to laser light. Considering also that a laser power ranging from 1 to 10 W, needs some minutes for a whole tumor-covering treatment, the risk of inducing undesired thermal damage to the healthy tissue and structures surrounding the tumor exists [4]. As a solution to reduce the amount of energy absorbed by healthy tissue in conventional methods, photothermal therapy (PTT) [5] has been proposed [6]. Here, photothermal agents are introduced in the tumor as light-absorbing materials to improve the efficacy of energy-to-heat transduction [7–9]. PTT employs near-infrared (NIR) laser photoabsorbers like metal nanoparticles (NPs) [9–12], carbon-based materials [13–15], organic compounds [16], indocyanine green [17], natural chromophores [18], and synthetic coordination polymers (eg, Prussian blue) [19,20] to generate the necessary heat for thermally ablating cancerous cells exposed to NIR laser irradiation. In particular, laser irradiation of noble metal NPs with localized surface plasmon resonances (LSPRs) in the first biological window (ie, 650-950 nm) has been widely investigated to achieve a potential clinically relevant photothermal effect [21]. Minimal invasiveness, high specificity, and precise spatial-temporal selectivity are some of the unique advantages of PTT in cancer therapy [22,23]. Furthermore, PTT can directly be used to eradicate the cells in primary tumors and it also can be combined with current therapeutic modalities to treat cancerous cells in the metastatic sites [24–29].

A combination of the targeted drug delivery systems with photothermal ablation offers the advantage of an enhanced therapeutic index, which can be especially significant in treating cancers with multidrug resistance [30,31]. For instance, an intelligent protoporphyrin-based polymer nanoplatform has been recently proposed as a new multifunctional NP for synergistic enhancement of cancer treatment through combined PTT and nitric oxide therapy, with a good therapeutic effect on drug-resistant tumors [32,33]. Chemo-photothermal therapy tuned to elicit anti-tumor immunity can exert striking therapeutic

effects against the primary tumors and the advanced metastatic cancers [34]. In this concern, several published reviews report either organic or inorganic nanomaterials for chemo-photothermal combination therapy [33,35,36]. A recent strategy that can be potentially applied in a variety of therapeutic agents with monitoring ability is represented by a multifunctional nanohybrid with two-photon excited fluorescence (TPEF) imaging performance and two-photon photothermal therapy (TP-PTT) effect [37].

Several approaches, such as radiotherapy or PTT, have shown significant progress on cancer treatments thanks to the unique electronic, optical, and chemical properties of gold nanoparticles (GNPs). GNPs allow achieving a significant therapeutic ratio when employed as radio or photosensitizing agents, in a proper concentration and dimension, within the tumor [16–20]. The therapeutic ratio, in this case, is related to the maximum radiation dose by which the death of cancer cells is locally controlled and the minimum radiation dose by which cells in healthy tissues have low acute and late morbidity [38–40]. Properties such as biocompatibility, chemical stability, inertness, relatively low cytotoxicity, thermal efficacy, and ease of detection make gold an eligible candidate to enhance PPT [41,42]. Moreover, the novel approaches for synthesis [5,43], as well as the application of GNPs as biomarkers and contrast agents (CAs) [44–46], and the progress in combinatorial cancer therapy pave the ways toward the theranostic use of GNPs in addition to PTT [6,47,48].

When the shape of GNPs changes from sphere to rod, the absorption and scattering wavelength will be shifted from visible to the NIR region, thus causing an absorption and scattering cross-section change. This variation allows them to be very efficient energy absorbers, at the desired light wavelength, able to generate a local temperature increase [49–52].

In the PTT scenario, rod-shaped GNPs, i.e., gold nanorods (GNRs), have been extensively investigated since they can strongly absorb electromagnetic waves at different frequencies corresponding to the NIR, leading to a rapid temperature rise of the host tissue [11,53]. Gold nanoshells (GNSs) are also largely employed as a NIR-responsive platform [54]. Indeed, gold-silica nanoshells have paved the way toward the first human application of PTT for the treatment of prostate disease [43,55].

The main challenge concerning GNPs-based thermal therapy consists in the delivery of an optimized concentration of NPs inside the target, sufficient to enhance the thermal effect while reducing laser intensity for sparing the healthy tissue [56]. Indeed, GNPs' optical properties, shape and size, coating, concentration, in association with laser wavelengths and powers [57–61], and tumor biological and chemical properties impact on the GNPs-

assisted PTT outcomes, as well as on the cell death mechanisms [5,48]. In this framework, also adequate tools for the planning and prediction of the GNPs-based thermal therapy settings, along with approaches for intraprocedural monitoring of the thermal outcome could provide a valid support for the design and control of the therapy.

Deepening the knowledge about the optical and thermal response of GNPs in both theoretical and experimental conditions is useful to better understand the settings and requirements for an optimal and effective PTT. By getting inspiration from interdisciplinary fields of science and technology, this review describes the fundamental aspects related to the GNPs-mediated PTT design. This work also provides essential information on the physical mechanisms underlying the heat generation induced by GNPs-mediated PTT. Indeed, insights on the phenomena describing laser-tissue interaction with GNPs are crucial for the pre-planning treatment design and for defining an accurate intraprocedural thermometric approach (Figure 1).

All the aforementioned aspects are at the basis of the actual translation of GNPs-mediated PTT from the laboratory to the clinical application.

2 | GOLD NANOPARTICLES

The use of NPs in diagnostic and therapeutic for cancers is rapidly expanding due to their unique properties such as small size, large surface area to volume ratio, high reactivity to the living cells, stability over high temperatures, and translocation into cells. Several studies have focused on high atomic number (Z) GNPs of different sizes, shapes, and surface coatings which offer different advantages, for example, being biocompatible, easily synthesizable and stable, as well as possessing the capacity to be internalized within cells and enhance radiation effects therein [62,63]. The specific property characterizing high-Z NPs is the enhancement of electron release in

the medium, due to atomic excitation by incident radiation. Moreover, GNPs can be functionalized with antibodies, polymers, and peptides for application in different fields [64–67].

Also, GNPs possess tunable optical properties and flexible surface chemistry. Their physical characteristics, such as surface plasmon resonance (SPR) and Raman scattering activity, make these NPs good candidates to be utilized as tumor-specific PTT agents, drug delivery vehicles, antiangiogenic agents or molecular reporters, and in further cancer therapy applications including optical imaging and photoacoustic tomography of tumors [44].

Therefore, if these particles can be preferentially delivered to tumor volumes, they can selectively increase the target's absorption, offering both improved image contrast and selective increases of the desired target's dose. However, the interaction between the cells and NPs as well as the way by which the NPs distribute within the body is an important issue which should be considered.

2.1 | Biodistribution and cytotoxicity of GNPs

Biodistribution and toxicity of NPs are mostly related to the way they are injected, that is, orally, intravenously, or directly into the tumor, and to their size. Nanomaterials composition is also a factor that determines the cellular uptake mechanisms and the intracellular localization of NPs, as well as their chemical interaction with cells [68].

By considering a major concern associated with the healthy tissues in NPs-mediated cancer treatment, different routes of NPs' administration, and the form and method by which the NPs disperse within the tissues after the injection, have been largely investigated and discussed [69–73]. Regarding the influence of the size, Hillyer and Albrecht investigated the gastrointestinal uptake and subsequent tissue/organ distribution of GNPs in mice for different orally administered NP's sizes, that is, 58, 28, 10, and 4 nm [74]. After the administration of
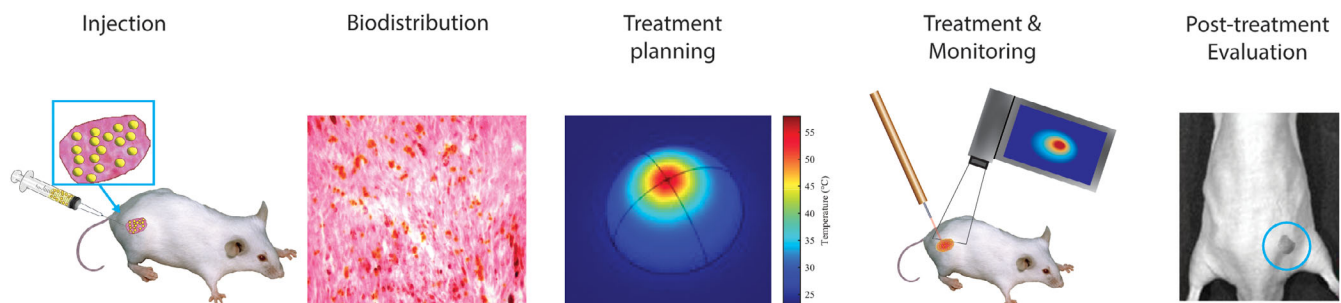

FIGURE 1 Schematic figure of the workflow of GNPs-based PTT

the particles, using transmission electron microscopy (TEM) and instrumental neutron activation analysis (INAA), they qualitatively and quantitatively measured the presence of gold in biological specimens. The smallest GNP's type (4 nm diameter) was observed in the kidney, liver, spleen, lungs, and even the brain, whereas the biggest one (58 nm diameter) was detected almost solely inside the gastrointestinal tract. They compared the presence of NPs in different organs and tissues such as blood, brain, lung, heart, kidney, spleen, liver, intestine, and stomach. Smaller colloidal GNPs were able to cross the gut and localize to tissues more readily than larger particles. NPs with size of 4, 10, and 28 nm were detected in the tissues they studied on. Regarding the GNP's size of 56 nm in diameter, in the majority of these tissues, gold was not detected. The paracellular mechanism of colloidal gold uptake they observed suggests that particles can enter the body without being subjected to organized intracellular processes such as lysosomal enzymatic degradation that may be deleterious to conjugated proteins or molecular species.

Oral and intravenous (i.v.) injections rely on the presence of leaky vasculature and enhanced permeation and retention effect (EPR; ie, passive targeting), which forces NPs to preferentially accumulate at the tumor site [75–78]. Several studies have shown less than 10% ID/g (Injected Dose/gram) of NPs delivered to the tumor when administered by intravenous injection [79,80]. In the i.v. injection of NPs, the main pathway of clearance is through the reticuloendothelial system (RES) via macrophages in the liver and spleen [80]. Thus, the decrease in the interaction between NPs and the RES lengthens the blood circulation time, and this longer period is often associated with higher intratumoral penetration [81].

Jong et al. compared the tissue distribution of various sized GNPs in the rat after i.v. injection through the tail vein and investigated the size-dependent organ distribution of GNPs [82]. Using the inductively coupled plasma mass spectrometer (ICP-MS) and TEM, they measured the presence of gold in different parts of the body 24 hours after the injection. The highest percentage of gold was found in the blood and liver, corresponding to 70% to 80% of the initial injection dose. The results showed that the majority of the NPs accumulate in the liver after i.v. injection irrespective of the NP's size.

The intratumoral (i.t.), that is, direct, administration of NPs with a reasonable dose by which the particles are directly introduced into the tumor site has shown successful results [83,84]. Kanavi et al. performed an ex vivo study on a fresh human whole eye enucleated for choroidal melanoma to investigate the distribution of GNPs within the eye after i.t. injection into the tumor. The results of this study proved the proper distribution of

GNPs within the tumor, while no particle was observed in the extratumoral areas [85]. Although this way of injection provides a more favorable GNPs' concentration inside the tumor while also decreasing the injection dosage, an i.v. injection could be more helpful in some cases, especially for tumors that are not accessible by direct injection of GNPs. Table 1 summarizes the main results of the biodistribution of GNPs in tissues.

Different nanomaterials induce different cell responses, resulting in variable toxicity [86–88]. The size and shape of particles, as well as the target cell type, are the critical determinants of the intracellular responses and the degree of cytotoxicity. In photothermal applications of GNPs, also changes in the geometry, surface conjugations, and administration methods play a key role in the cytotoxicity and biodistribution of GNPs [89,90]. The cytotoxicity data, which can be obtained through different assays, help predict the NPs' biocompatibility [91,92].

Some works have suggested the dependency of GNPs' cytotoxicity on the adopted doses and stabilizers [93,94]. Furthermore, the variation of the GNPs' cytotoxicity in human lung and liver cancer cell line suggests its dependence on the cell type [95]. Nonmalignant cells have shown to be more sensitive to these NPs than cancerous cells [96].

Regarding GNPs, the majority of research has been conducted on the cellular uptake and cytotoxicity of GNSs [97–102], whereas a few investigations have been performed in the presence of GNRs [103, 104]. Recently, a comprehensive systematic study has been done on the influence of GNPs' size, shape, and surface coating on cellular uptake and cytotoxicity [105].

Although many studies have shown negligible cytotoxicity for GNPs [101, 106, 107], the available literature in this field contains conflicting data since the diverse cell lines, various cell viability assays, and different chemical routes employed to synthesize GNPs [103, 108], together with the absence of standard safety protocols.

For instance, some studies have reported that GNSs are less cytotoxic than GNRs, and in another study, GNRs showed less toxicity than GNSs [89,108,119].

Sun et al. have reviewed the cell death induced by GNPs focusing on apoptosis, necrosis, autophagy, and associated molecular mechanisms [102]. By considering different sizes, they compared the relationship between GNPs' properties and cell death for a variety of cancer types. It was concluded that the small-sized GNPs induced more necrosis, hexagonal GNPs, and GNRs induced more apoptosis compared to the spherical-shaped NPs and finally the hydrophobic and charged GNPs induced higher apoptosis and autophagy levels than the hydrophilic and neutral charged GNPs, respectively.

TABLE 1 Biodistribution of GNPs in different tissues

Study	Concentration	NPs	Time After Injection	Size [nm]	Blood	Brain	Lung	Heart	Kidney	Spleen	Liver	Pancreas
					[ng/g$_{Tissue}$]							
Mice Oral [74][a]	2×10^5 ng$_{gold}$/ g$_{water}$	GNSs	12 hours	d: 4	6.83 ± 0.69	4.67 ± 0.26	32.42 ± 9.37	15.05 ± 2.05	75.40 ± 10.65	20.25 ± 2.27	21.27 ± 3.62	—
				d: 10	0.77 ± 0.07	2.06 ± 0.78	8.55 ± 4.90	7.27 ± 3.25	17.36 ± 1.51	7.01 ± 4.65	2.78 ± 0.30	—
				d: 28	0.47 ± 0.20	0.70 ± 0.20	0.80 ± 0.35	1.51 ± 0.78	6.19 ± 1.51	13.74 ± 13.48	1.16 ± 0.03	—
				d: 58	0.09 ± 0.10	2.40 ± 1.30	−1.43 ± 0.37	−2.37 ± 0.86	1.46 ± 0.33	0.65 ± 1.20	0.37 ± 0.16	—
Mice i.v. [83]	1.8×10^2 ng$_{GNRs}$/g	GNRs@PEG	Day 1	L: 25 ± 3 W: 5.5 ± 0.8	—	—	~3	—	~5.8	~74	~10.2	—
			Day 3		—	—	~2.7	—	~2	~76	~8.5	—
			Day 7		—	—	~1.85	—	~2	~69	~8.1	—
			Day 14		—	—	~1.6	—	~2	~65	~7.9	—
			Day 30		—	—	~1.25	—	~1.5	~54	~87.8	—
Mice i.v./i.p. [119]	1×10^4 ng$_{GNPs}$/ g$_{body\ weight}$	i.v. TCOOH	24 hours	Core d: 2	—	174	32 737	—	3600	43 100	154 800	2632
		i.v. TTMA			—	268	2339	—	2800	22 700	30 800	660
		i.v. TEGOH			—	441	6471	—	4500	36 800	84 500	2063
		i.p. TCOOH			—	4800	25 500	—	21 080	86 900	130 700	288 400
		i.p. TTMA			—	4700	26 400	—	21 040	110 200	96 600	218 200
		i.p. TEGOH			—	4800	39 900	—	20 160	46 100	117 200	151 600

[a]The results are expressed ± Standard Error.

In the experimental study by Connor et al., GNPs with different sizes and capping agents have been investigated for the uptake and cytotoxicity in human leukemia cells. They used MTT assay to evaluate the cytotoxicity of GNPs, and the results suggest that spherical GNPs with a variety of surface modifiers are non-toxic to cellular function despite being taken up into cells [101].

Khlebtsov and Dykman have presented a detailed analysis of data published between 1995 and 2010 on the in vitro and in vivo biodistribution and toxicity of most popular GNPs after i.v. injection, including atomic clusters and colloidal particles of diameters from 1 to 200 nm, GNSs, GNRs, and gold nanowires [81].

In the field of PTT, Moustafa and colleagues have recently summarized the progress toward a better understanding of the efficacy, mechanism, and toxicity of GNPs-assisted PTT of cancers [110]. They have made an in-depth comparison of different shapes and sizes of GNPs based on the amount of heat generation. In this comparison, higher heat generation efficacy, longer blood retention, and higher i.t. penetration are reported for the smaller sizes of GNPs ($\leq$20 nm). However, particles with larger size ($\geq$ 20 nm) have shown lower toxicity rather than the smaller one.

In the study of the PTT ablation properties of GNRs, systematical evaluation of the cytotoxicity and cellular uptake behavior of these particles show the high dependency of cellular behavior on both the NPs' surface coating and the cell type [111].

GNRs have limited clinical use due to the cytotoxicity caused by the surfactant like cetyltrimethylammonium bromide (CTAB) that serves as a template during the GNRs' synthesis process. In this regard, Mooney and coworkers have employed GNRs coated with 11-Mercaptoundecyltrimethylammonium bromide (MUTAB) instead of CTAB, for in vivo PTT purposes on xenograft tumors. The adopted MUTAB-coated GNRs resulted to be cytocompatible up to a threshold of approximately 3 mg/mL [112]. Furthermore, another strategy is the surface modification with polymers, which is suggested to reduce such surfactant-related cytotoxicity [113].

Regarding all the above-mentioned cases about the restriction of the clinical usage of NPs in cancer therapy, numerous studies and researches have been done to develop new methods for the treatment of cancer with potential translation to the clinic. However, the delivery of NPs into the tumor site, their biological distribution, lack of clearance from the systemic circulation, inherent toxicity, and off-target effects are still significant restrictions that bridge the gap between laboratory and clinical usage of NPs [114, 115]. Indeed, a further concern is related to the long-term fate of the delivered GNPs and

the associated long-term cytotoxicity. Although solid knowledge of the systemic effects arising from the clustering and accumulation of GNPs is missing, the first investigations seem to indicate GNPs' superficial charge and dimensions as crucial aspects [6,116]. Moreover, the preferential accumulation sites appear to be the liver and spleen, as shown by Goodrich and colleagues, which observed foreign bodies in 100% of livers and 7 out of 8 spleens in murine models. Conversely, no foreign bodies were found in the brain, heart, lung, kidney, adrenal gland, or mesenteric lymph nodes, after administration of PEGylated GNRs (length = 44.7 ± 5.4 nm and width = 14.3 ± 1.8 nm) [117]. Due to the limited period of observation related to animal studies, typically up to 6 months from the administration [6], the available data are not sufficient to estimate the actual GNPs' long-term cytotoxicity, hence further investigations are needed to assess their behavior in broader time intervals.

2.2 | Delivery of GNPs

Microenvironmental characteristics such as high stroma density and high interstitial fluid pressure can impede the efficient delivery of NPs into the tumor [118]. In the case of hypovascular tumors, the delivery of NPs through the EPR effect alone is not very efficient and most NPs localizes predominantly in the mononuclear phagocytic system [119–121]. The biological barriers, detrimental to the final effectiveness of the delivery system, which nanomaterials might encounter from the site of injection to the site of action are generally summarized in blood barriers, tumor barriers, and cellular barriers [122, 123].

Regarding the tumor barrier, pathological features of vascular and stromal barriers, as well as their influence on the delivery efficacy, have been recently described, and the strategies for engineering NPs to overcome these challenges have been outlined [124].

Image guidance combined with minimally invasive interventional procedures has been recently widely studied as a method able to simplify regional drug delivery, targeted vascular embolization, and direct tumor ablation. Interventional oncology includes different minimally invasive methods with real-time image-guided procedures for the diagnosis and treatment of cancer with the advantages of lower costs, fewer complications, and faster recovery times in comparison to surgery [125, 126].

Li and colleagues have reviewed the current image-guided interventional cancer nanotheranostics with specific attention to their applications for the management of pancreas cancer. This method allows the possibility of disrupting the stromal barrier of pancreatic ductal adenocarcinoma (PDAC) [127].

Considering their nanometric dimensions, NPs' entry is easily facilitated into various cells, posing one of the greatest difficulties in using them for targeted delivery to specific tissues. This problem can be prevented by actively targeting NPs to receptors or other surface membrane proteins overexpressed on target cells. For this aim, NPs are functionalized by conjugating with targeting ligands, that have an inherent ability of directly selective binding to cell types. Regarding GNPs and their biomedical applications, some reviews have been done to indicate the enormous growth in this field [128–131].

Antibodies, antibody fragments, aptamers, peptides, and whole proteins (eg, transferrin) and different receptor ligands (eg, folic acid) are some of the targeting ligands employed to actively target GNPs [132]. For target delivery with each kind of the present ligand, the surface of NPs should be chemically modified to introduce reactive parts, thereby providing functional group that can be conjugated to them to allow for selective delivery of the desired NP therapeutics. Some reactive groups utilized in chemical reactions for conjugating NPs to targeting ligands are listed and available [133].

Cheng et al. have explored the relationship between tumor delivery efficiency and NP-specific parameters by analyzing the reported data from 2005 to 2018 related to a wide range of NPs, including GNPs, through the physiologically based pharmacokinetic (PBPK) models. The factors influencing tumor delivery kinetics have been identified, and they found that a low delivery efficiency is associated with low distribution and permeability coefficients at the tumor site [134].

In the critical revision of the PTT concept based on the intravenous-targeted delivery of GNP, quantitative tumor uptake studies for a class of GNRs conjugated to tumor-targeting peptides are reported [135]. The application of GNPs' conjugates in biomedical diagnostics and analytics, PTT as a carrier for delivering target molecules, and the immunological and toxicological properties are reviewed by Dykman and colleagues [136].

In the in vitro and in vivo study on the chemo-physical properties and PTT effects of GNRs, Liao and colleagues fabricated NIR-stimulated polymersomes, artificial vesicles that can co-deliver GNRs for cancer therapy. This system presents a useful strategy for maximizing the therapeutic efficacy and minimizing the dosage-related side effects in the treatment of solid tumors since they can be efficiently taken up by the tumor cells. The heat from the GNRs not only promotes drug delivery into the tumor, but also increases the drug toxicity to tumor cells [113].

In another recent study, triphenylphosphine (TPP) surface-functionalized and F-108 Pluronic-stabilized GNPs, presenting a new compound (F-108@TPP-AuNPs) with unique properties like water stability, TPP-controlled release, photostability, high light-to-heat conversion capabilities, were proposed. In the in vivo and in vitro trial on Hela cells, this compound, when exposed to irradiation, showed superior anticancer activity through apoptosis mechanism due to the synergism between chemotherapy and hyperthermia with a clear advantage of the combined vs individual therapies [137].

In cancerous cells, the set of transcribed genes is changed compared with non-cancerous cells, leading to an elevated pool of specific messenger RNAs (mRNA). Several mRNAs are transcribed by ribosomes in the endoplasmic reticulum in proximity to the cell nucleus. These agglomerations of mRNA around the nucleus can be a unique target in the tumor. A combination of NPs and RNA is intended to enhance the safe delivery of the desired target and sometimes it is used to silence the target mRNAs [138].

In the review by Xiao et al., the NPs-based RNA delivery systems which are currently approved for clinical trials in cancer therapy are listed and available [139].

2.3 | Stabilization of GNPs

In addition to the functional groups, surface-bound ligands also contribute to the stability of NPs, leading to effective interaction with cancer cells. Stabilizing agents are used to maintain the stability of NPs under harsh conditions like in the cell or in the bloodstream. They also prevent aggregation of NPs, improve their stability in water solutions, and change their bioavailability in biological systems [140, 141]. Furthermore, the NPs' coating impacts structural stability and prevents quenching [142].

Although there is considerable progress in the field of biomedical application of GNPs, the stability of these particles in the physiological conditions remains unclear.

At the cellular level and by interacting with the cell membrane, mitochondria, or nucleus, GNPs with different capping may behave in different ways. A detailed comparative analysis of the role of different surface capping material on the stability and toxicity of three water-soluble GNPs is provided in [143].

Although GNRs are known to be promising agents for PTT, their uptake is lower than GNSs. Proper stabilizing agent can be selected to provide effective penetration of these particles into cells [144].
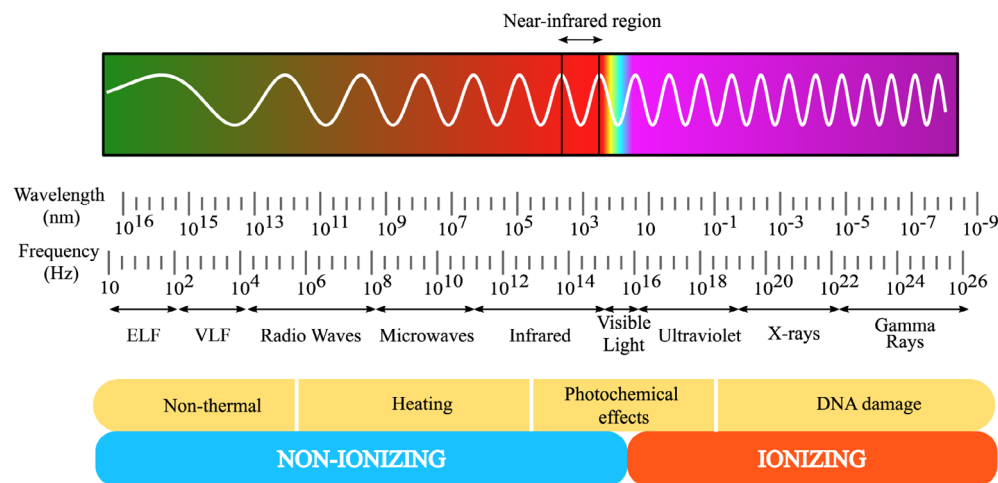
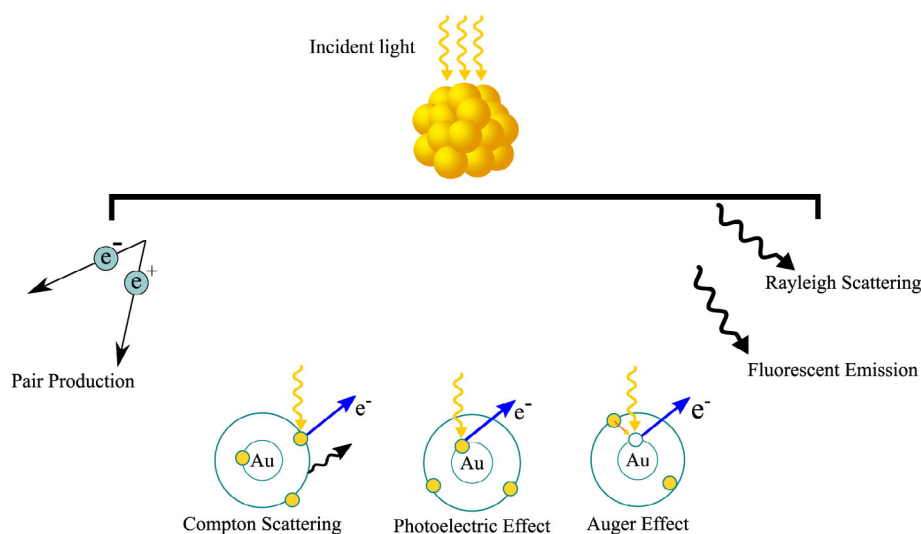**FIGURE 2** Types of electromagnetic radiations and their effects

FIGURE 3 Schematic illustrating potential interactions of incident photons with a gold atom (the target can be another high-Z material)

3 | PHOTONS INTERACTION WITH GNPS

3.1 | Electromagnetic radiation

In terms of the modern quantum theory, electromagnetic radiation (EMR) is the flow of photons (light quanta) in the space. The effects of EMR on the chemical compounds and biological organisms are dependent on the power and frequency of radiation. In terms of frequency, EMR is classified as being non-ionizing (longer wavelength/lower frequency/lower energy) and ionizing (shorter wavelength/higher frequency/higher energy; Figure 2).

Individual photons of the high-frequency beam, like ultraviolet (UV), X-rays, and gamma rays have enough energy to ionize atoms, molecules, or break chemical bonds. For this reason, they can cause damage in living cells and can be a health hazard. In the case of high-Z

nanoparticles, like GNPs, according to the energies of ionizing photons, different interactions might occur when the particles are exposed to radiation (Figure 3).

In contrast, lower frequencies EMR (radiowave, microwave, infrared [IR], and visible light) constitute the non-ionizing radiation: the individual photons do not have enough energy to cause ionization or break of chemical bonds. Radiation in this category affects living tissue and chemical system because of the heating effects due to the combined energy transfer of many photons.

3.2 | Surface plasmon resonance and optical response of GNPs

Nowadays, there is an increasing interest in the electromagnetic properties of metal-dielectric interfaces dating back to the work of Gustav Mie (1908) and Rufus Ritchie (1957) on small size metal particles. When the size of

FIGURE 4 Scheme of light interacting with a metallic NP. The electric field of light induces the movement of conduction electrons, which accumulate at the NP surface, creating an electric dipole and an electric field opposite to one of the light
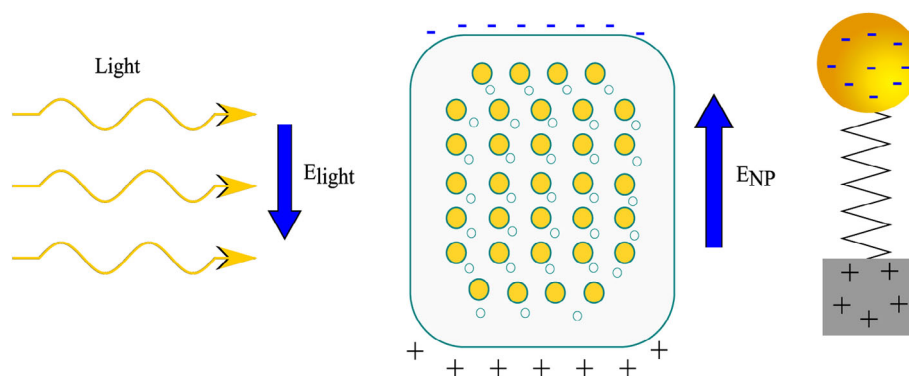
metallic particles is reduced to the nanometer range, the optical properties are modified by the appearance of surface plasmon (SP) and their behavior becomes completely different than the bulk metal one. SP is the coherence delocalized electron oscillation existing at the interface between two materials, where the real part of the dielectric function changes the sign across the interface [145].

Metallic NPs have conduction electrons confined to a finite volume, which is defined by the particles' dimensions, and move almost freely inside them. When these particles are exposed to the non-ionizing radiation, the electric field of incident light penetrates the NPs and polarizes the conduction electrons, thus exerting a force on these electrons moving them toward the surface of particles. As a result, negative and positive charges accumulate in two opposite sides creating an electric dipole that generates an electric field inside the particles opposite to that of the light. This electric field forces the electrons in returning to the equilibrium position. Thus, the displacement repetition causes the electrons to oscillate (plasma oscillation) at a frequency called plasma frequency (Figure 4).

Only the light with the same frequency of this oscillation can excite the plasmon (a quantum of plasma oscillation), in which the resonance occurs in electrons (SPR) [146–148]. Through this excitation, the energy of the light is transferred to the plasmonic nanostructure and the light is quenched due to the dissipation of the energy into the metal NPs as heat instead.

The SPR condition depends on the size, shape, structure, dielectric properties of the metal, and of the surrounding medium [49,52,146–148]. Plasmons in the metallic nanostructure (NPs with size much smaller than photon wavelength) are non-propagating excitations (ie, localized excitations), so they are known as LSPRs because the resulting plasmon oscillation is distributed over the whole structure.

LSPRs manifest themselves as a combined effect of scattering and absorption in the optical extinction spectra [149]. This characteristic is strongly dependent on the

morphology, size, and composition of particles, as well as on the local dielectric environment.

The LSPR of a metal NPs is sensitive to the nearby medium where the other metal NPs might be present, acting as a perturbation factor for a dielectric ambient. When the particles are placed at a distance of a few nanometers apart, the light-induced dipole moments of the particles couple to each other, giving rise to the noticeable variation in absorption as well as scattering cross-sections of the adjacent particles [150]. Such a plasmonic coupling offers a unique strategy to tune the optical scattering and absorption cross-sections of the system.

Optical extinction is defined as a rate of local energy losses caused by the particle (absorption in the particle volume and scattering by the particle-matrix interface) referenced to the matrix background.

The oscillation increases the kinetic energies associated with the electric fields of the dipole. Given that the total energy should be constant (law of conservation of the energy), this increase of energy will be provided by the illuminating light.

As it was mentioned above, when NPs are illuminated at their plasmonic resonance, the SP is excited inside them and the light partially extinguishes. The larger the electron oscillations, the larger the light extinction. The optical absorption spectrum allows detecting the excitation of SP. While the excitation in the SP induces absorption of light, some of the incident photons will be released with the same frequency and energy in all directions. This phenomenon is known as the process of scattering.

The surface plays a crucial role in the observation of the SPR. Change in surface area can alter the boundary conditions for the polarizability of the metal and, therefore, can shift the resonance to optical frequencies. The change in the size and shape of the NPs affects the SPR processes and, consequently, the NPs' optical properties. For instance, spherical NPs made of gold and silver have a strong SPR band in the visible region (Figure 5) [151].
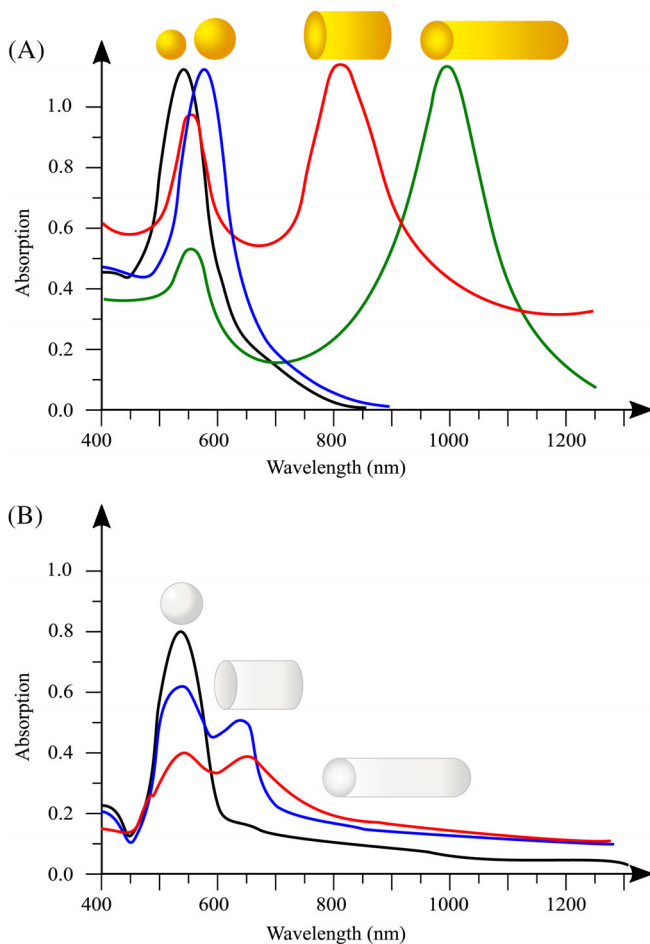
FIGURE 5 Schematic comparison of the size and shape effects on metal NPs' absorption at different wavelengths: A, GNPs and B, Silver NPs

Comparing to the solid structures, hollow or core-shell NPs show a red-shifted band of the LSPR wavelength. Anisotropic shapes such as rods, triangles, and branched structures also show a red-shifted SPR band compared to the spherical analogs, in nanoscale particles. For instance, GNPs in different shapes and structures like GNRs, silica/gold nanoshells, and hollow GNPs exhibit larger red-shift properties that have boosted their value in PTT [152, 153].

To design NPs for biomedical applications, it is important to know how the NPs' spectra change in a physiological environment. In the systematic study by Chen et al. [154] on metal NPs based on optical spectra changes in the cellular environment, they quantified changes in the peak wavelength of gold spectra when GNPs are introduced to human breast cancer cells. They showed that when 100 nm GNPs are exposed to Sk-Br-3 breast adenocarcinoma cells, an average shift of approximately 79 nm in the optical spectra can be achieved. Spectral shift is dependent on both the time and NP exposure dose. When the incubation time increases, the cells have a chance to process NPs into larger endosomal vesicles containing multiple NPs, thus causing a continuous shift for the spectra with time. Furthermore, the time at which the NPs are optically excited should be considered. Indeed, at shorter incubation times following NP exposure, smaller shifts were observed. For instance, for 100 nm GNP introduced to the mentioned cells, the peak wavelength in the spectra stays within 30 nm of its initial peak wavelength in the first 2 to 5 hours of incubation, but it shifts significantly between 10 and 24 hours.

Quantitative analysis and characterization of spectral broadness change after interaction with cells will help guide NP design for maximal efficacy and safety in biological environments.

3.3 | GNPs as photothermal agents

Due to the SPR excitation, the light absorption by GNPs is strongly enhanced, being almost 5 to 6 orders of magnitude larger than the absorption of dye molecules [155]. The absorbed light is further converted into thermal energy, thus exerting a localized temperature increase.

Among the first studies, the work by El-Sayed et al. showed the efficiency of GNSs as a photothermal agent near its plasmon resonance absorption (ie, 530 nm) when they irradiated epithelial carcinoma cells with a 514 nm laser [156].

However, spherical GNPs absorb only UV and visible light. Since the penetration of UV and visible light is limited by tissue (the penetration of UV radiation and light into human tissue is limited by scattering and absorption, the scattering increases with decreasing wavelength), they are not a good choice for tissue heating.

The optimum wavelength for high tissue penetration is ~800 nm [157] (Figure 6); therefore, some new nanomaterials have been designed recently to expand the absorption band to the NIR region [41]. This has been done by altering the shape and size of NPs for potential PTT.

When the shape of GNPs is changed from spheres to rods, GNRs display two characteristic transverse and longitudinal SP absorption bands. Electron oscillation can occur in one of two directions depending on the polarization of the incident light. If the oscillation occurs along the long axis, a strong SP absorption band in the NIR region is induced and referred to as longitudinal band. When the oscillation occurs along the short axis, a weak absorption band in the visible region, and at a wavelength like that of GNSs, is induced. That is typically referred to as transverse band. While the transverse band is insensitive to the size changes, the longitudinal band is
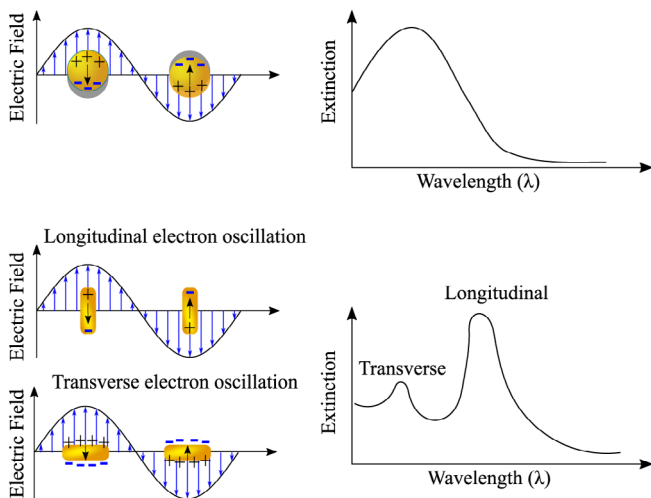
FIGURE 6 Interaction of polarized light with GNSs and GNRs

red-shifted largely from the visible to NIR region with increasing aspect ratios (AR = Length/Width) [158].

Pointing out that the metal NRs can be usually considered as a prolate spheroid, which is certainly a good approximation, this optical behavior can be well understood according to Gans theory [159] (Appendix 1).

According to the report by Link and El-Sayed [160, 161], a linear proportional relationship between the longitudinal SPR absorption maximum (λ_{max}) and the AR of NRs: $\lambda_{max} = 95(AR) + 420$ can be observed.

As the AR increases, the SPR maximum is linearly red-shifted. Such optical behavior is different from spheres for which the SPR only slightly red shifts with increasing particle size. In summary, when the SPR is excited within the particles, the total light extinction includes both absorption and scattering. In the Gans theory, the total extinction of the light (C_{ext}) is determined as the sum of the absorption (C_{abs}) and scattering (C_{sca}) cross-sections. The resonance wavelength can be estimated considering the dielectric constant of the metal ($\varepsilon_1 + i\varepsilon_2$) and the surrounding medium (ε_m), the polarization factor, the three axes of nanoparticles, and the AR [162, 163].

At such a wavelength, absorption, scattering, and total extinction increase, hence promoting the use of GNRs for therapeutics and biomedical imaging applications. The frequency of the SPR is tunable by changing the $\varepsilon_m(\omega)$ of the surrounding medium, but it is also strongly affected by NP size, shape, and composition.

In the dielectric constant, the imaginary part ($i\varepsilon$) is associated with dielectric losses, and the real part (ε_1) is an indication of the degree of polarization. The greater the degree of polarization, the greater the value of ε_1. The dielectric constant is a function of frequency. As the

frequency increases, the value decreases due to polarization mechanisms no longer being able to follow the rapidly changing field. The imaginary part is always positive and represents the loss factor or energy absorbed.

In GNRs, the absorption and scattering are dependent on both the wavelength and the AR. This issue was well studied by Lee et al. [164]. They investigated the effects of shape, size, and AR on the optical absorption and scattering in these NPs. According to their results, the relative contribution of optical scattering to the total extinction of GNRs was found to greatly increase with a slight elongation of the sphere (the AR becomes slightly above 1 for the particles having the same total number of gold atoms).

Regarding the heat generation, when the NIR radiation reaches the GNRs, the energy of the light absorbed by the GNRs is transferred into heat, making them good candidates for photothermal treatment of cancers. The light absorption results in an increase in particle temperature caused by the LSPR decay in which excited electrons couple within the NP. The generated thermal energy is quickly transferred to the NP environment through phonon-phonon coupling and the heat increase around them leads to a local temperature rise of tens or hundreds of degrees above physiological temperature [165]. The extent of the temperature increase depends on the laser energy and the absorption cross-section of the GNRs at the laser wavelength.

Considering that the absorption and scattering properties of GNPs are dependent on wavelength and AR, the amount of heat generated by NP can be controlled by the size, shape, concentration and the aggregation state of the NP, as well as by the power, wavelength, and the time duration of the light source. Thus, the laser-particles interaction allows heat management in addition to the optimization of the local electromagnetic field [52,166,167].

Several studies have been done on the optical properties of GNRs and implementations in cancer PTT. Huang and colleagues provided an in vitro demonstration of GNRs as a CA for photothermal cancer therapy. They conjugated GNRs to the anti-EGFR as a receptor specified for the epidermal growth factor and bind them to the different malignant and non-malignant epithelial cells. Exploiting the strongly scattered red light from GNRs in the dark field, they could visualize and distinguish the malignant cells from the nonmalignant ones during microscopy. Additionally, they irradiated these cells with a laser wavelength of 800 nm and investigated the photothermal destruction effects of NRs. This work demonstrated the potential use of GNRs as a novel CA for imaging and photosensitizer agent for PTT of cancer cells using NIR laser [61].

Mooney et al. performed an in vivo study on flank xenograft tumors to assess the photothermal effects of GNRs in laser therapy of cancers. They considered different powers for laser source and different concentrations for GNRs to compare the influence of these factors on the temperature reached in the surface of the tumor (T_s) and intra-tumoral parts (T_{IT}). They reported a significant increase in the difference between T_s and T_{IT} when the concentration is changed. They also showed the influence of laser power on these temperatures [112].

Regarding the influence of the size on the amount of heat generated by GNRs, the diameter of 10 nm and the length of 40 nm, for GNRs represent one of the most common sizes that have been utilized in PTT, because in this size longitudinal plasmon resonance occurs around 800 nm [168, 169].

Mackey et al. compared the efficacy of GNRs in PTT of cancers for different dimensions with the AR of 3.4, 3.45, and 3.5. They used theoretical calculation as well as an in vitro experimental approach to determine the optimum size in this regard. Comparing three different sizes of GNRs, the size of 28 nm in length and 8 nm in diameter resulted in the most effective CA for PTT of human oral squamous cancerous cells, when the cells were exposed to continuous wave (CW) laser (808 nm) at 5.8 W/cm² (spot size around 5.6 mm). This size was reported as an optimum size that has the best compromise between the total amount of absorbed light and the fraction of which is converted into heat [169].

3.4 | Morphology changes of irradiated GNPs

The physical and chemical properties of NPs are dependent on their shape and size [170]. According to the characteristics and the energy of the source, irradiation of NPs may influence their morphology and structure, thus leading to a modified interaction with light during irradiation (Table 2).

Brigs et al. have reviewed how ionizing radiation environments affect the structure and properties of GNPs. They also focused on the effects of neutron, beta, alpha, and heavier charged particles irradiation on GNPs. Interactions of radiation with elemental gold are highly dependent on the species of the incident radiation. As a result of ionization and Coulombic interaction, heavy ions can transfer much more energy to the gold atoms they interact with, which causes large displacement damage cascades. In comparison to charge particles, neutrons have a high mean free path (average distance traveled before interaction) owing to the lack of Coulombic interaction. Thus, no significant damage events could be expected for a vast majority of neutrons interacting with GNPs [171].

Concerning non-ionizing radiation, Link et al. compared the morphology changes in GNRs after laser pulse irradiation for two different time durations. Results showed that, at lower pulse energy, reshaping of GNRs mostly occurs for femtosecond compared to nanosecond laser pulses. Indeed, for a certain number of photon irradiation, the laser beam can heat the lattice much more effectively and more rapidly in the short pulse rather than in the longer pulse. The rate of heating the lattice is faster than the rate of cooling in the shorter time scale so that the cooling, which occurred in this duration (femtosecond), could not compete with the rate of absorption and excitation [172].

Significant changes in the morphology (reshaping from rod to sphere and particle size reduction) have been observed in the GNRs when they are exposed to high-intensity pulsed-lasers at different wavelengths. These changes in the geometry of GNRs causes a shift in the peak of optical absorption [173–175].

Chou et al. have shown that after irradiation of GNRs with 146 mW CW laser, the heating decreased after 5 seconds. This evidence suggested a possible shape change in the particles occurring after the specific heat process [176].

Setoura et al. experimentally investigated the morphological changes in a single GNS when it is exposed to focused 488 nm CW laser irradiation in air and water media [177]. They compared the size change in a GNS with a diameter of 102 nm for different exposure times (125 μs-5 s) and power intensities (10-60 mW·μm⁻²). The laser intensity-dependent particle changes showed that the threshold associated with size reduction is more clearly defined in water than in air. Because of higher thermal conductivity in water compared to the air, the laser-intensity-dependent increase in particle temperature has a much smaller slope. The onset of diameter reduction in this experiment was reported to be at 1 to 5 seconds of irradiation, that is, the threshold intensity of bubble formation, that is, ~16 mW·μm⁻². It means that from the evaporation of surrounding water caused by heat transfer from the NP, the bubbles are formed. This can result in a sudden jump in the temperature of NP surrounded by the bubble, due to the poor thermal conductivity of air. In a certain exposure time and at a higher power density, the higher size change was reported for both water and air media.

The consequence of using CW laser on the morphology of GNRs was demonstrated in the in vitro and in vivo study by Harris-Birtill et al. [178]. They compared the absorbance and the spectral peak for GNRs with different optical density before and after exposure to the laser

TABLE 2 Change of morphology in GNPs after PW and CW laser irradiation

NPs	Laser settings		Size before irradiation	Size after irradiation
NR [172]	PW λ: 800 nm F: 0.001 J/cm^2 τ: 100 fs		AR: 4.1 L: 44 nm W:11 nm	AR: 4.1 L: 44 nm W:11 nm
	PW λ: 800 nm F: 0.64 J/cm^2 τ: 7 ns			Reshaping of several NPs to odd (φ) shape particles
NR [174]	PW λ: 532 nm F:67.4 mJ/cm^2 Single Pulse		AR: 6.1 ± 3.4 d: 21.7 ± 6.1 nm V: 6169 ± 3680 nm^3	AR: 6.5 ± 2.9 d: 19.0 ± 4.9 nm V: 5340 ± 2494 nm
	PW λ: 1064 nm F: 42.5 mJ/cm^2 Single Pulse			AR: 5.2 ± 1.5 d: 17.8 ± 4.1 nm V: 5101 ± 2436 nm
	PW λ: 1064 nm F: 18.5 mJ/cm^2 2000 shots			AR: 4.6 ± 0.9 d: 20.4 ± 5.4 nm V: 4779 ± 2754 nm
NR [175]	PW λ: 1064 nm P: 750 mW f: 20 Hz		AR: 5.0 ± 1.2 L: 49.6 ± 9.7 nm W: 10.6 ± 3.2 nm	AR: 1.7 ± 0.9 L: 27.0 ± 8.2 nm W: 17.2 ± 3.7 nm
NR [178]	PW λ: 808 nm F:18.5 mJ/cm^2 f: 1 Hz τ: 7 ns		AR: 3.8 ± 0.5 L: 43.1 ± 7.7 nm W: 11.5 ± 2.3 nm	AR: 3.3 ± 0.8 L: 42.1 ± 6.8 nm W: 13.3 ± 2.2 nm
	CW λ: 808 nm F:12 W/cm^2 t: 45 s			AR: 2.3 ± 0.8 L: 35.8 ± 6.6 nm W: 16.2 ± 2.6 nm
	CW λ: 808 nm F:6 W/cm^2 t: 300 s			AR: 2.9 ± 0.9 L: 39.5 ± 7.5 nm W: 14.4 ± 2.5 nm
	CW λ: 808 nm F:6 W/cm^2 t: 300 s		AR: 3.9 ± 0.6 L: 44.3 ± 4.9 nm W: 11.6 ± 1.2 nm	AR: 2.8 ± 1.0 L: 34.8 ± 8.2 nm W: 13.4 ± 2.8 nm
NS [177]	CW λ: 488 nm t: 10 ms In Water	Pd: 10 mW/μm^2	d: 112 ± 4 nm Include the Pt-Pd alloy layer of 5 ± 2 nm	d ≈ 110 nm
		Pd: 20 mW/μm^2		d ≈ 78 nm
		Pd: 30 mW/μm^2		d ≈ 74 nm
		Pd: 40 mW/μm^2		d ≈ 60 nm
	CW λ: 488 nm t: 10 ms In Air	Pd: 10 mW/μm^2		d ≈ 111 nm
		Pd: 20 mW/μm^2		d ≈ 95 nm
		Pd: 30 mW/μm^2		d ≈ 80 nm
		Pd: 40 mW/μm^2		d ≈ 65 nm

beam. By using TEM and spectroscopy, changes in the dimension and AR of GNRs were assessed for each sample (Figure 7).

The results of this study demonstrated a significant decrease in the length of GNRs, which caused a shift in the spectral peak toward the blue in addition to a decrease in the absorption of the LSPRs at the laser wavelength after irradiation of all samples (GNRs with different optical densities). Reshaping of GNRs after the initial laser application subsequently leads to prolonged irradiations ineffective and unlikely to provide any additional clinical effect due to irreversible change in their optical absorption properties. So, evaluation of the NRs morphology is good to be considered during the in vivo thermal therapy studies in conjunction with light fluence to better appreciate the implications on tumor response, especially when this method of therapy is being contemplated for therapeutic tumor regression.

4 | TISSUE-LASER INTERACTION IN THE PRESENCE OF GNPS

4.1 | Interaction between tissue and laser

Biological tissues are complex optical properties landscapes composed of different structures and compartments. Cells, vasculature, interstitial spaces, each possessing various properties and attributes, influence the overall tissue optical behavior, thus absorption and scattering result far different from other bulk materials [179].

Reflection, refraction, absorption, scattering, and fluorescence are the basic phenomena occurring in living tissues when they are irradiated by laser light and each biological tissue has individual impulse response functions [180–184]. Since tissue is a dielectric medium, whose average refractive index (RI) is higher than that of air [185–187], the light interacting with the tissue surface can undertake partial reflection at the tissue/air interface, while the remaining part penetrates the tissue [188, 189].

Multiple scattering and absorption processes in the tissue are responsible for broadening and eventual decay of the light beam as it travels through tissue, while a large fraction of radiation is dispersed in the backward direction for bulk scattering [187]. Therefore, light propagation within tissue depends mostly on the scattering and absorption properties of its components (various cells and fiber structures). The size, shape, and density of these structures, their RI, and the polarization state of the incident light predetermine the character of light propagation in tissues [190]. The photons of incident laser diffuse and attenuate in the tissue when the light is scattered by the cells, nuclei, mitochondria, lysosomes, macromolecules, membranes, and other components. The behavior of laser in its interaction with tissue and other structures can be classified based on its wavelength since the scattering and molecular absorption are wavelength dependent. For instance, the 200 nm wavelength is slightly absorbed by viruses, incrementally increasing into bacteria and mammalian cells, respectively. The 630 nm wavelength is absorbed by the mitochondria and oxygen consumption is activated by illuminating with light at 365 nm [191]. Therefore, the wavelength of laser has an important role in medical optics due to the absorption peaks of biomolecules and tissues and can have a significant impact in normal and malignant tissues (Figure 8).

In the study by Germert et al., the optical properties of normal and cancerous human liver were
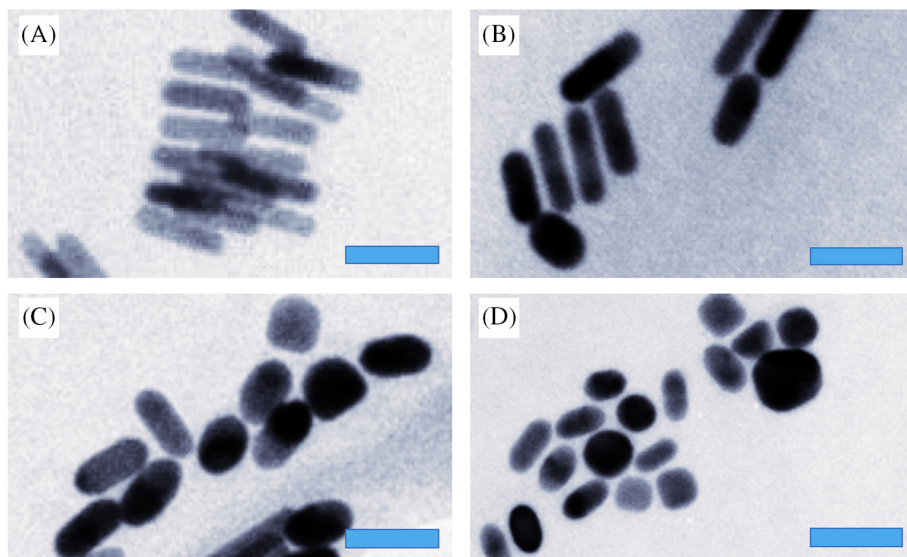

FIGURE 7 TEM image (from Reference [179]) showing the size change in NRs after laser irradiation. A, Before laser irradiation; B, After pulse laser light; C, After 6 W/cm^2 CW irradiation; D, After 12 W/cm^2 CW irradiation. The blue scale bars represent 50 nm
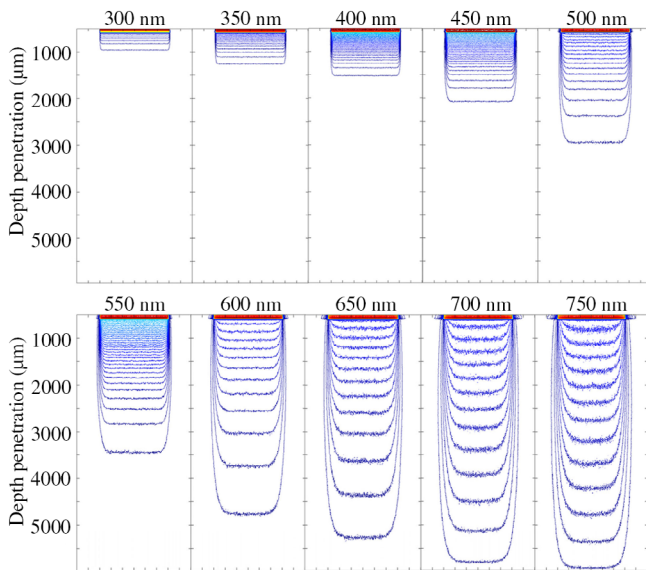
FIGURE 8 Penetration of 300 to 750 nm photon into tissue matrix from the photon distribution (from Reference [289])

investigated for different wavelengths in the NIR range. The scattering coefficient of the healthy liver tissue was showed to be significantly higher than in metastatic tissue at three wavelengths of 850 nm, 980 nm and 1064 nm (20.4 mm^{-1} vs 10.8 mm^{-1} at 850 nm; 18.2 mm^{-1} vs 11.3 mm^{-1} at 980 nm; 16.9 mm^{-1} vs 10.9 mm^{-1} at 1.064 nm). The absorption coefficient of the healthy liver was also higher than in metastatic tissue (0.10 mm^{-1} vs 0.06 mm^{-1} at 850 nm; 0.08 mm^{-1} vs 0.06 mm^{-1} at 980 nm; 0.05 mm^{-1} vs 0.03 mm^{-1} at 1.064 nm). Subsequently, the penetration depth in the healthy tissue was lower than in the cancerous liver (1.8 mm vs 2.3 mm at 850 nm; 2.2 mm vs 2.7 mm at 980 nm; 3.0 mm vs 4.2 mm at 1.064 nm) [192].

Optical absorption in biological tissue originates mostly from water, hemoglobin, and melanin. In the visible range, absorption of light is insignificant for most tissues except for the absorption bands of blood hemoglobin and some other chromophores [193, 194]. In the IR region, the absorption is essentially defined by the water content. Water has two regions of strong absorption: in UV and in the NIR regions. The absorption bands of protein molecules and nucleic acids are mainly in the near-UV region with the absorption peaks at 260 to 280 nm. Hence, in the UV region, the laser light is strongly absorbed by water and proteins in the tissue, resulting in poor light penetration.

For this reason, the range of NIR from 650 to 1350 nm is defined as the therapeutic window, that is, the wavelength range in which light has its maximum depth of penetration within biological tissues.

For different human tissues and tissue components, RI, in the visible/NIR range varies from a value slightly higher than for water, due to the influence of some organic components, to RI $\cong$ 1.35 for interstitial fluid and 1.62 for tooth enamel.

Different tissue parameters governing the optical absorption and scattering are summarized and available in the works by Jacques and Tuchin [195, 196].

The parameters of irradiation like wavelength, energy, and exposure time can be matched to specific physical, chemical, and biological properties of the target tissues to get the desired result. Tissues also can be defined by their optical properties (absorption and scattering), thermal properties (heat capacity and heat diffusivity), mechanical properties (viscoelasticity, tensile strength and rupture points), chemical composition (water and other endogenous and exogenous absorbers), anatomy (physical arrangement of organelles, cells, and tissues), and physiology (tissue and organismal metabolic status and function). Depending on the conditions mentioned above and the desired endpoints, some properties will dominate over others as the major determinants of the final effects of laser-tissue interactions.

Photobiological interaction and the reaction mechanisms between the lasers and living tissues were first systematically presented by Boulnois in 1986 [197]. By considering the time, Boulnois classified the mode of laser-tissue interaction into four groups: *electromechanical interaction* (exposure times from 10 ps to 10 ns); *photoablative interaction* (l0 ns to 100 ns pulses, UV); *thermal interaction* (1 millisecond to 10 seconds exposure, quasi-CW); and *photochemical interaction* (10-1000 seconds, quasi-CW).

Photomechanical effects refer to tissue damages resulting from mechanical compressive or tensile forces generated by the rapid introduction of energy into heat with short laser pulses (<1 μs, electromechanical interaction, and photoablative). In this case, the shape of the material is changed when it is exposed to light. Photochemical effects (low-level light therapy is attributed to photochemical interactions) depend on the absorption of light to initiate chemical reactions such as the production of reactive chemical species in photodynamic therapy. Photothermal effects (thermal interaction) result from the transformation of absorbed light energy into heat, leading to coagulation or destruction of the target tissue. The high-power densities reached on sub-millimeter spot sizes provide spatially localized heating used in the thermal mode of interaction, forming the well-known basis of all surgical applications.

The thermal and photobiological effects of laser-tissue interactions are complex and result from some phenomena: conversion of light into heat, transfer of heat within

the tissue, and tissue reaction. Photothermal injuries on tissue and their dimensions depend on tissue temperature and the heating time. The pathological changes in tissue also depend on the functional anatomy and biology of the tissue, the photobiological mechanism of injured tissue, and the immediate, short-term, and long-term, responses of the cell or organism to the injury over time. The pathological photothermal effects are well analyzed and described by Thomson [198].

Laser ablation, used to make incisions or resections, serves as the basis of all photosurgical or photocoagulation applications belonging to the thermal interaction mode. Thermal injury is dependent not only on the thermal history but also on the inherent tissue thermal properties [199]. Water predominates as a major determinant of the thermal properties of most soft tissues. On the other hand, in hard tissues such as bone and dental enamel, its influence may be less important. When the tissue absorbs the light, the energy of laser irradiation is converted into heat and transferred to the tissue components, DNA/RNA, chromophores, proteins, enzymes, and water. The interest in this application of laser energy for tumor removal is mostly raised by its technical feasibility: the use of fine needles (eg, 21 gauge) for the introduction of the laser-delivering fibers into the tumor, allows nodules to be treated in difficult locations with a reduced risk of procedural complications.

The temperature certainly is the governing parameter of all thermal laser-tissue interactions, and to predict the thermal response of the tissue, a suitable model for the temperature distribution inside the tissue must be derived. Different mathematical and computational modeling has been done to estimate and analyze the temperature distribution and thermal damage [3,200–203].

4.2 | Tissue-laser interaction and heat transport in the presence of GNPs

The light transport is described by the radiative transport equation (RTE) [128], [129]

$$\vec{\Omega}\nabla I_\lambda\left(\vec{r},\vec{\Omega}\right) + \beta_\lambda I_\lambda\left(\vec{r},\vec{\Omega}\right) = \frac{\mu_{s,\lambda}}{4\pi}\int_{4\pi} I_\lambda\left(\vec{r},\vec{\Omega}'\right)$$

$$\phi_\lambda\left(\vec{\Omega}',\vec{\Omega}\right)d\vec{\Omega}' + S\left(\vec{r},\vec{\Omega}\right) \quad (1)$$

where I_λ is the spectral radiation intensity in position $\vec{r}$ and direction $\vec{\Omega}$, which varies according to the extinction caused by absorption and scattering coefficients, as well as from the scattering phase function ϕ_λ in and from other directions. $S\left(\vec{r},\vec{\Omega}\right)$ is the source term related to an isotropic interior photon source density, which can be neglected in the case of low radiation emission by scattering and absorbing medium. β_λ is the extinction coefficient of the medium, usually used to describe scattering media in optics, and given by the following expression:

$$\beta_\lambda = \mu_{a,\lambda} + \mu_{s,\lambda} \quad (2)$$

where $\mu_{a,\lambda}$ and $\mu_{s,\lambda}$ are the absorption and scattering coefficients of the medium, respectively.

Tissue properties, laser fluence, and thermal response will be altered when the NPs are introduced to laser therapy.

To solve the equation for the specific absorption rate (SAR; Appendix 1, Equation (9)) for laser heating of NPs, several approximations have been used and compared directly to experimental results. P1 approximation and variations (taking the first term of Fourier series of radiative intensity field) [204], diffusion approximation (taking the first two terms of energy radiance which is expressed as a series of spherical harmonics) [205], two-flux approximation (equivalent to the zero-order approximation of the double spherical harmonics), Monte Carlo (modeling the trajectory of a large amount of light rays) [205] are some of the approximations used to model the light transport [206].

According to the two-flux approximation proposed by Dombrovsky et al. to solve the RTE model [207], $\mu_{a,\lambda}$ and $\mu_{s,\lambda}$, for a composite medium (ie, biological tissue) containing a volume fraction f_v of NPs (when f_v is small compared to the volume of the host matrix, that is, around 10^{-6}-10^{-5}%), are defined as in the following equations:

$$\mu_{a,\lambda} = \mu_{a,t} + \mu_{a,NPs} = \mu_{a,t} + 0.75\cdot f_v\cdot\frac{Q_{abs}}{r_{eff}} \quad (3)$$

$$\mu_{s,\lambda} = \mu_{s,t} + \mu_{s,NPs} = \mu_{s,\lambda} + 0.75\cdot f_v\cdot\frac{Q_{scat}}{r_{eff}} \quad (4)$$

where $\mu_{a,t}$ and $\mu_{s,t}$ are the absorption and scattering coefficients of the hosting tissue, and r_{eff} is the effective radius of nanoparticles. Q_{abs} and Q_{scat} are the dimensionless efficiency factor of absorption and scattering for a single particle, related to the absorption and scattering cross-sections according to the following relations:

$$C_{abs} = \pi\cdot r_{eff}^2\cdot Q_{abs} \quad (5)$$

$$C_{sca} = \pi\cdot r_{eff}^2\cdot Q_{scat} \quad (6)$$

In the case of GNRs, the following electrostatic approach based on the Mie theory has been proposed by Soni and co-workers [208]. This approach is often exploited to

characterize the optical coefficients when NPs having a diameter less than 100 nm are irradiated within the NIR wavelength range [145]. The electrostatic approach states that for a NP with a diameter $d \leq \frac{\lambda}{10}$, being λ the wavelength of the incident radiation, the NP itself is subject to a uniform electric field and the particle can be described as a dipole with induced oscillations [209]. In case of GNRs, having a diameter of d [nm], length l [nm] and dielectric function ε, embedded in a medium constituted by biological tissue of dielectric function ε_m, the polarization of the GNRs along the three axes affects the final optical coefficient values. The terms indicated as a_1, a_2, a_3 represent the GNRs polarizations along the x, y, and z axes, respectively. The term a_i was introduced to describe the general equation of the polarization of GNRs along the i axis:

$$a_i = 4\pi d^2 l \left(\frac{\varepsilon - \varepsilon_m}{3P_i(\varepsilon - \varepsilon_m) + 3\varepsilon_m} \right) \quad (7)$$

in which P_i indicates the geometric factor.

The absorption and scattering coefficients of the gold GNRs embedded in a medium containing a volume fraction f_v of GNRs are given by the following equations:

$$\mu_{a,GNRs} = \frac{2\pi f_v}{\lambda V_n} imag \left(\frac{a_1}{3} + \frac{a_2}{3} + \frac{a_3}{3} \right) \quad (8)$$

$$\mu_{s,GNRs} = \frac{16\pi^3 f_v V_n}{18 \lambda^4} \left(|a_1|^2 + |a_2|^2 + |a_3|^2 \right) \quad (9)$$

More in detail, the heat transfer in biological media is described by the following equation, firstly presented by Pennes in 1948, who validated this model by performing different experimental studies [210, 211]:

$$\rho \cdot c \cdot \frac{\partial T}{\partial t} - \nabla(k\nabla T) = Q_v \quad (10)$$

where T is the tissue temperature as a function of space and time, Q_v is the volumetric heat source, k is material thermal conductivity, c is specific heat and ρ is the density.

If Q_e, Q_m, and Q_s are considered as the terms related to the heat exchange due to water evaporation, metabolic heat generation, and external heat source, respectively, the thermal response of tissue to the heat source that is crucial to understand the principle of thermal treatment can be modeled by the Pennes (or bioheat) equation:

$$\rho \cdot c \cdot \frac{\partial T}{\partial t} = \nabla(k\nabla T) + \rho_b \cdot c_b \cdot w_b \cdot (T - T_b) + Q_m - Q_e + Q_s \quad (11)$$

in which ρ_b is the blood density, c_b refers to the blood specific heat, and w_b is defined as the amount of blood perfused per unit volume per second or blood perfusion rate per volume unit. The term T_b concerns the blood temperature of the region that is not subject to the treatment. The term Q_m represents the oxidative process-associated heat generation: lipids, proteins, and carbohydrates undergo oxidative processes, which are related to a subsequent heat generation [112]. The term Q_e refers to the tissue internal water evaporation during heating. As a matter of fact, during heating, when temperature approaches high values, tissue water content is lost through evaporation. The gas pressure is subsequently increased in the region where the evaporation process takes place and the water vapor tends to diffuse toward regions of the tissue characterized by lower pressure values. These areas are not only characterized by lower pressure, but also by lower temperature values so that vapor changes its physical state into water, releasing its latent heat, which is further able to increase the temperature in that area [212].

The term Q_s is the external heat source generated by laser light absorption.

Beyond a simplified approach based on the use of SAR for the definition of Q_s, several models have been used to describe the light-tissue interaction phenomena, responsible for the heat generation Q_s, also in the presence of GNPs [207, 213, 214].

When tissue is illuminated with a laser, the energy of the beam is absorbed by the chromophores such as water, melanin, and blood leading to a temperature rise in the tissue. This energy can be assumed as a heat energy source, $Q_s(r, z, t)$, inside the exposed tissue. The deposition of heat in the tissue is due only to light that is absorbed in the tissue. For a light flux in the z-direction in a non-scattering medium, the local heat deposition per unit area and time is given by:

$$Q_s(r,z,t) = -\frac{\partial I(r,z,t)}{\partial z} \quad (12)$$

When a simplified approach based on the Lambert-Beer law is employed for the macroscopic description of the GNPs-enhanced laser therapy, the $I(r,z,t)$ term, dealing with the absorption of photons occurring during the interaction of monochromatic electromagnetic radiation with tissue, can be modeled by:

$$I(z) = I_0 \cdot e^{-\beta_k \cdot z} \quad (13)$$

where $I_0 = P/\pi r^2$ is the laser intensity, P is the laser power, and r is the radius of the beam. This relationship, also known as Lambert-Beer law, is valid under the

hypotheses that $\mu_{s,\lambda} = NC_{sca} \ll 1/L$, where N is the scatters density number, and L is the media thickness.

The transfer of heat through tissues embedding NPs, which is essentially produced by the mechanism of conduction, will tend to enlarge the volume of primary heat energy source $Q_s(r, z, t)$. Conduction may transfer energy by interaction with tissue particles. This transfer occurs randomly between the more and the less energetic particles and results in a secondary heated volume that is bigger than the primary source, which is based only on the conversion of light into heat. The secondary heated volume should be considered when studying the denaturation of tissue.

The spatial extent of heat transfer is described by the time-dependent thermal penetration depth (z_{therm}) as an essential parameter that is defined as a distance in which the temperature decreases about 63% of its peak value.

$$z_{therm}(t) = \sqrt{4Dt}, \text{with } D = \frac{k}{\rho c} \qquad (14)$$

where D is the tissue thermal diffusivity, k is the temperature conductivity, and c is the specific heat.

The time during which heat energy can diffuse inside the tissue, that is, the relaxation time (τ_{therm}) is an indication of the tissue thermal susceptibility. τ_{therm} is the time taken by the target to dissipate about 63% of the incident thermal energy and is related to size of target. Additionally, τ_{therm} is a function of extinction coefficient and, consequently, of the optical penetration depth, L; this last term is the distance in which $I(z)$ has decreased to 63% of its peak value or is dropped to $1/e$ of its incident value I_0 and is related to the absorption coefficient ($L = 1/\mu_a$). Therefore, L can be equated to z_{therm}:

$$L = \frac{1}{\mu_a} = z_{therm} = \sqrt{4\alpha\tau_{therm}} \qquad (15)$$

$$\tau_{therm} = \frac{1}{4\alpha\mu^2} \qquad (16)$$

In the case of a pulsed laser, for duration $t < \tau$, the thermal energy cannot diffuse to the distance given by the optical penetration depth; so, thermal effects can be negligible. For $t > \tau$, the heat can diffuse up to the multiple of the distance given by the optical penetration depth, therefore thermal effects or damages are possible.

According to the data calculated by Hale and Query for the absorption of water based on the wavelength, and regarding the z_{therm}, the shortest thermal relaxation time of approximately 1 μs occurs at the absorption peak of water near 3 μm [215]. Based on these equations, a theoretical model describing the thermal response of laser-irradiated tissue was used to evaluate the temperature distribution as a function of time [180, 216, 217].

5 | TEMPERATURE MONITORING TECHNIQUES

Transportation of thermal energy or heat transfer in biological tissues involves different mechanisms such as thermal conduction, convection, blood perfusion, radiation, metabolic heat generation, and phase change [218, 219].

Depending on the duration and peak value of the tissue temperature achieved, different effects like coagulation, vaporization, carbonization, and melting may be distinguished. According to the degree of heating, thermal damage can be categorized into:

- 42°C to 45°C: the beginning of hyperthermia, conformational changes, and shrinkage of collagen.
- 50°C: reduction of enzymatic activity.
- 60°C: denaturation of proteins, coagulation of the collagens, and membrane permeabilization.
- 100°C: tissue drying and formation of vacuoles.
- >100°C: beginning of vaporization and tissue carbonization.
- 300°C: thermoablation of tissue, photoablation, and disruption.

Both tissue temperature and the amount of thermal damage depend on the laser wavelength and power, the treatment time, the thermal properties of treated biological tissues, as well as the GNP absorption cross-section, which is the property governing absorption of laser light by a GNP [56].

Real-time thermometry can aid to prevent unintended damage by providing an accurate image or trend of the temperature distribution in the tissue undergoing the procedure, as well as useful feedback to adjust therapy.

In the last decades, several thermometric techniques have been proposed to improve the efficacy of ablation-based treatments in research, and more recently in the clinical settings [220, 221].

Thermocouples, IR thermal imaging, and magnetic resonance thermometry (MRT) are mostly used to measure temperature during different types of cancer treatment [221–224]. Techniques like computed tomography-thermometry, photoacoustic thermometry, fiber Bragg grating (FBG) sensors are emerging for real-time temperature and related thermal-damage control [225]. An overview of these techniques and their application during GNPs-based photothermal

therapy are presented in the following paragraphs and resumed in Table 3.

It is worth mentioning also another branch called Nanoscale Thermometry, which focuses on the intracellular thermal sensing, based on both nanothermometers and imaging. Techniques used for nanoscale thermometry in cells undergoing GNPs-mediated PTT are described in these two excellent reviews [206, 226].

5.1 | Sensor-based techniques

Fiber optic sensors (eg, fiber Bragg grating [FBG] and Fluoroptic sensors), and thermocouples (TCs) are two main classes of thermometers used in in vivo thermal treatments [220, 227].

Fiber optic sensors are small-sized, immune to electromagnetic interference, therefore usable in magnetic resonance imaging (MRI) and computed tomography (CT) systems, flexible, biocompatible, and suitable for minimally invasive temperature measurement [221, 228]. Fiber optic sensors are good candidates for in vivo temperature measurements because they do not cause immune responses in the hosting body [228]. The main advantage of the use of FBGs over fluoroptic sensors and TCs are the multiplexing capability, which allows for a chain of several sensors embedded in one single fiber, and the absence of measurement artifacts due to the direct light absorption. Custom FBGs can be written in thin fibers (diameter < 250 μm), with a sensing length of single grating ranging from <1 to 10 mm, and with a short edge-to-edge distance (<0.3 mm) between consecutive sensors, providing quasi-distributed temperature measurement along with the fiber length [229]. The spatially resolved thermometry performed by a single fiber permits reduced invasiveness and the detection of the effective thermal increase due to the medium-embedded NPs, as recently proposed in Reference [230].

Temperature monitoring by TCs is a conventional and well-developed technique, which is widely used since it is a cost-effective, has acceptable accuracy for the application and a wide measurement range. Furthermore, TC's small size and the fast response in time make them suitable for localized temperature monitoring. Contrary to FBGs, one TC can perform only single point measurement, so, for temperature mapping, several thermocouples must be inserted, thus increasing the invasiveness. Moreover, a strong absorbance of the laser radiation by metallic TCs and their high heat conduction and direct light absorption could entail a temperature measurement error [231–235].

When referring to sensors for temperature monitoring during GNPs-mediated PTT, most of the authors use TCs, mostly because of their large availability. Dickerson et al. used extracorporeal irradiation assisted with GNRs, and hypodermic TC placed at the tumor center [53]. Goodrich et al. also monitored the treatment with GNRs with TC placed under the tumor, using a rectal probe with a thermometer for body temperature measurements [117]. Mooney et al. employed a pair of TCs to measure tumor internal and superficial temperature for different laser and GNRs settings, and compared the in vivo outcome with numerical simulations [236].

5.2 | Image-based techniques

With the aim to overcome the drawback of the invasiveness of sensors and to achieve distributed measurements, the temperature is also collected by imaging systems. Systems able to correlate tissue emitted light with its thermal state, such as IR thermal camera, and diagnostic images relying on temperature-dependent tissue properties, such as MR, CT, ultrasound (US), photoacoustic (PA) imaging are widespread. MR, US, CT, and PA-thermometry can measure temperature distribution inside the tissue, whereas IR thermography can only monitor the surface temperature of biological tissue.

IR thermography is a contactless method relying on the detection of IR energy emitted by a body and on its conversion into a thermal image. The system is affordable and easy to use with respect to other image-based techniques, but it can retrieve surface-temperature only (Figure 9A) [237, 238]. Its large availability makes IR thermography one of the most used approaches for assessing the efficacy of GNPs-mediated PTT. Terentyuk et al. provide in vivo analysis of the thermal efficacy of silica/gold nanoshells, with the temperature resolution of 0.15°C. They performed an investigation of heating kinetics, spatial temperature distribution, and morphological alterations in the tissue dependent on laser irradiation parameters and NPs' concentration. Wang et al. used the IR thermography for comparing the photothermal conversion efficiencies of different types of gold nanostructures and for studying the photothermal cancer treatment efficacies of PEGylated GNPs in a tumor model following i.v. administration [239]. Mirrahimi et al. validate an alginate nanogel co-loaded with cisplatin and GNPs for combined chemo-photothermal therapy in a murine model, and performed real-time temperature measurements by means of IR thermography [240].

MR-thermometry is considered the current clinical gold standard for 2D-3D tissue temperature mapping in the organs. Among all available techniques, the method based on proton resonant frequency (PRF) shift method

TABLE 3 Laser therapy assisted with GNPs: (A) Clinical trials, (B) in vivo experiments, and (C) in vitro and ex vivo studies

(A) Clinical trials

Study typology	Laser setting P (W) Pd (Wcm^{-2})	λ (nm)	t(s)	Nanoparticles Type	Size (nm)	Injection mode	Injection quantity	Target	Temperature measurement method	Therapy outcome
Safety Clinical Study [55]	P: 3 to 5 (CW), laser energy delivered by a 400 mm core optical fiber, 1-cm long isotropic diffuser	810	180-240	Gold-silica nanoshells (GSNs)	d: 150	i.v.	7.5 mL/kg (~2.77 × 10^{11} particles/mL)	Prostate cancer	Thermocouple to monitor the anterior wall of the rectum adjacent to the prostate	No temperature increase was measured. No significant long term effect on the patients' chemical balance or metabolism. Two adverse effects: one allergic episode and one burning sensation.
Pilot Clinical Study [43]	P: 4.5 to 6.5 (CW), patients treated with 10-mm or 18-mm optical fiber diffuser	810	180 (5 to 52 excitations)	Gold-silica nanoshells (GSNs)	d: 150	i.v.	7.5 mL/kg (~2.77 × 10^{11} particles/mL)	Prostate cancer	—	Results after 3 months: Prostate volume decreased from 49 to 42 cm^3; PSA decreased from 6.7 to 3.9 ng/mL; PSA density decreased from 0.137 to 0.083 ng/cm^2. Therapy was successfully achieved in 94% (15/16) of patients.

(B) in vivo studies

Study model	Laser setting P (W) Pd (Wcm^{-2})	λ (nm)	t (s)	Nanoparticles Type	Size (nm)	Injection mode	Injection quantity	Target	Temperature measurement method	Therapy outcome
Canine and feline [84]	Pd: 5.8 (CW), laser beam spot size ~2.7 mm in diameter	808	120-300	GNRs@PEG	W: 5 L: 25	i. t.	7.5 nM/100 cm^3 of tumor volume	Mammary gland adenocarcinoma (MCF-7), variant tumor volumes (~1-20 cm^3)	33-gauge hypodermic thermocouple	All 13 tumors regressed with an average half-life of about 2 weeks and completely disappeared within 6 to 8 weeks. No relapse or toxicity effect even 1 year after treatment.
Rat [237]	P: 2, Pd: 4, total E: 120 J (CW), P:	810	10-360	Silica/gold Nanoshells	d: 140 (core)/20 (shell)	Sub then (within	0.1 mL of NS solution	Skin and Muscle white rat tissues	Thermal Camera	Control: reached 46°C in 3 to 4 min.

TABLE 3 (Continued)

(B) in vivo studies

Study model	Laser setting				Nanoparticles		Injection mode	Injection quantity	Target	Temperature measurement method	Therapy outcome
	P (W) / Pd (Wcm^{-2})	λ (nm)	t (s)		Type	Size (nm)					
	8, on-off time ratio of 0.25, and pulse duration of 1 msec (PW)				(NSs)@PEG		20 min) i.M	(0.150 mg/mL of gold)			Tissue treated with NSs: reached 46°C in 15 to 20 s. Fast and prolonged self-limited temperature rise with PW.
Murine [117]	P: 3.5 (CW), a cooled optical diffusing fiber with an isotropic diffusing tip of 1 cm was also used	808	180		GNRs@PEG	Aspect ratio: 0.32	i. t.	6 mL/kg body weight (~2.6 × 10^{12} particles/ mL)	CT26.wt Murine colon carcinoma, tumor diameter of ~7 mm	Hypodermic thermocouple placed under the tumor and parallel to the laser fiber. The body temperature recorded using a rectal probe.	Liver, spleen, and lymph nodes exhibited substantial GNR accumulations. Maximum temperature in tissue of 62°C for the NRs-assisted therapy, and a maximum temperature in tissue in the laser-only control animals of 45.3°C. The survival of the photothermally treated group was statistically longer than the control groups, with approximately 44% tumor free through the evaluation period (60 days post-treatment).
Murine [284]	P: 5 (CW), laser beam spot size of 30 mm in diameter	807	600		Gum Arabic-encapsulated GNPs (GA-GNPs)	d: 15-18	i. p.	0.03 mg/100 mL per mouse	Lung carcinoma, tumor induced by diethylnitrosamine (CCL4, used as promoting agent)	—	Mice scarified and immediately scrutinized to collect lung tissues after 1 month from the treatment: GA-GNPs showed no cytotoxicity in the absence of laser light, the combination of GA-GNPs with laser induced cell death in lung tumor tissues with a reduction in the inflammation and angiogenesis together with an elevation in lipid peroxidation.
Murine [283]	Pd: 0.5 (CW), laser beam spot size	808	60		Hollow GNSs@ PEG attached with α-melanocyte-stimulating	mean d of 43.5 ± 2.3 and mean shell thickness of 3 to 4	i. v.	2.5 × 10^{12} particles per mouse	Murine melanoma (B16/F10)	—	Irradiation with GNSs decreases the metabolic activity in the tumor. Selective photothermal

(Continues)

TABLE 3 (Continued)

(B) in vivo studies

Study model	Laser setting P (W) Pd (Wcm⁻²)	λ (nm)	t (s)	Nanoparticles Type	Size (nm)	Injection mode	Injection quantity	Target	Temperature measurement method	Therapy outcome
	of 10 mm in diameter, light dose of 30 J/cm²			hormone analog (NDP-MSH-PEG-HAuNS) and hollow GNSs@PEG						destruction of the target tumors mediated by NDP-MSH-PEG-HAuNS was confirmed histologically (using excised tissue) and functionally ([18F] fluorodeoxyglucose PET imaging).
Murine [236]	Pd: 2 (CW), laser beam spot size of 15 mm in diameter Pd: 3 (CW), laser beam spot size of 15 mm in diameter	810	30, 60, 120, 300 300	GNRs	GNR dimensions corresponding to a peak absorption at 808 nm	i. t.	Injected GNR masses: 0.0125, 0.025, and 0.05 mg	Human breast cancer (MDA-MB-231)	Two thermocouples (K-type), Thermal Camera	No burns for control. Skin burns with GNRs. Significant differences between internal and surface temperatures: this difference increases with NP concentrations, decreases with laser P, and is not influenced by treatment time. Results suggest that tumor resorption requires intratumoral temperature over 50°C for more than 3-4 min.
Murine [53]	Pd: 0.9-1.1 (CW), laser beam spot size of 6 mm in diameter Pd: 1.7-1.9 (CW), laser beam spot size of 6 mm in diameter	808	600	GNRs@PEG	L: 50 W: 12	i. t. i. v.	0.015 mL of GNRs@PEG solution (OD$_{\lambda = 800\ nm}$ = 40) 0.1 mL of GNRs@PEG solution (OD$_{\lambda = 800\ nm}$ = 120)	Squamous cell carcinoma (HSC-3), tumor diameter of 3 mm	33-gauge Hypodermic Thermocouple	Tumor resorption >57% of the directly injected tumors and 25% of the intravenously-injected tumors (observation of inhibition of average tumor growth over a 13-day period)
Murine [239]	Pd: 1.0 (CW), spot size adjusted to cover the entire tumor area Pd: 1.2	808	300 600	Gold nano hexapods (GNHs)@PEG GNRs@PEG Gold nano cages (GNCs)@PEG	Core d: 25.3 ± 0.9 Arms L: 16.3±2.2 Arms W: 13.6 ± 1.8 L: 36.2±2.3 W: 9.1 ± 1.7 Edge L: 47.4 ± 4.5	i. t. i. v.	0.04 mL of 1 nM GNHs 0.2 mL gold nanostructures	Breast cancer (MDA-MB-435)	Thermal Camera	Maximum temperature (55.7 ± 2.4°C) for GNHs with highest photothermal conversion efficiency. Decrease in tumor standardized uptake values for all the three NPs.

TABLE 3 (Continued)

(B) in vivo studies

Study model	Laser setting P (W) Pd (Wcm⁻²)	λ (nm)	t (s)	Nanoparticles Type	Size (nm)	Injection mode	Injection quantity	Target	Temperature measurement method	Therapy outcome
	(CW), spot size adjusted to cover the entire tumor area				Inner Edge L: 37.1 ± 2.7 Wall Th: 5.2		solutions (gold atom mass of ~0.8 mg per mouse)			Reduction in tumor metabolism in mice treated with GNHs/GNRs: 90%, and with GNCs: 80%.
Murine [240]	Pd: 1.1 (CW)	532	900	Alginate nanogel co-loaded with cisplatin and GNSs nanocomplex	hydrodynamic diameter of 20-80	i. p.	0 mg/mL for control; 1 mg/kg cisplatin, 5 mg/kg gold	CT26 Mouse colon adenocarcinoma, average tumor volume of ~150 mm³	Thermal Camera	Temperature > 45°C for tumor treated with laser and NPs. Tumor growth suppression up to 95% of control and markedly prolonged animal survival rate due to the combined action of chemo-photothermal therapy using the nanocomplex. 60% of mice revealed no evidence of recurrence until the end of the 45 days follow-up period.
Murine [259]	Pd: 1.3 (CW)	808	600	Gold nano-shelled microcapsules (GNS-MCs)	2320 ± 1070	i. t.	0.2 mL, 10 mg/mL suspension	Human breast cancer (BT474), tumor volume of ~400 mm³	Thermal Camera, thermometer	Laser irradiation increased the intratumoral temperature to nearly 70°C for 8 min in GNS-MCs-treated mice. Tumor volumes decreased gradually and tumors resulted completely ablated in 6 out of 7 mice by 17 days after treatment.
Murine, FEM simulation [112]	P: 2.1, 3 PD: 1.4, 2 (CW), laser beam spot size of ~14 mm in diameter	810	300	GNRs	W: 10 L: 41	i. t.	0.0125, 0.025, and 0.05 mg of GNR/0.02 mL	Human breast cancer (MDA-MB-231), tumor volume of 123 mm³	Two thermocouples (K-type)	Difference between intratumoral and superficial temperature substantial when GNRs are injected. Maximum temperature reached influenced by both P and GNR concentrations. Tumors heated above 55°C experienced regression.

(Continues)

TABLE 3 (Continued)

(B) in vivo studies

Study model	Laser setting P (W)	Pd (Wcm⁻²)	λ (nm)	t (s)	Nanoparticles Type	Size (nm)	Injection mode	Injection quantity	Target	Temperature measurement method	Therapy outcome
											Good agreement between experimental and theoretical intratumoral temperature (maximum difference of 4°C).
Phantom [244]	P: 2.24 (CW)		532	240	GNSs	d: 5-15	Phantom loaded with NPs	0 for control, 0.008, 0.016 mg/mL	Agar Phantom	MR-Thermometry, Thermal Camera	Temperature reached at the center of phantom: 27.2, 37.8, 45°C. Total area of heat distribution: 94.9, 452.16, 907.34 mm².

(C) in vitro and ex vivo studies

Study model	Laser setting P (W)	Pd (Wcm⁻²)	λ (nm)	t(s)	Nanoparticles Type	Size (nm)	Injection mode	Concentration	Target	Temperature measurement method	Therapy outcome
Phantom, FEM simulation [245]	P: 1, 2 (CW)		521, 528, 535, 549, 560 / 843	300	GNSs / Silica/gold nanoshells (NSs)	d: 10, 20, 40 / d: 70	Phantom loaded with NPs	0 for control, 0.008, 0.016 mg/mL	Agar phantom	MR-Thermometry	Maximum temperature (51°C) for d: 20 nm GNSs, 0.016 mg/mL, P: 2 W. Reasonable correlation between simulation and MR-thermometry (R = 0.92).
Cell culture [286]		Pd: 0.5, 1, 2, 4 (CW)	810	1800	GNRs	L: 29.1±0.8, W: 8.8±0.2	Cells treated with NPs	~0.02 mg/mL	Human myeloid leukemia (OCI AML3)	Thermal Camera	Pd: 2 identified as ideal for selective destruction of cancer cells: temperature 46.4±1.9°C, apoptotic 8 days after irradiation in the presence of NPs.
Cell culture [287]	P: 0.2 (CW), laser beam spot size of 1 mm		808	90, 105, 120, 135, 150, 165, 180, 195, 210, 225, 240	GNRs (different surface modifications: PEG, phosphorylcholine (PC), folic acid	L: 30.4, W: 8.4	Cells treated with NPs	0 for control, 0.005, 0.010, 0.015, 0.020, 0.025 mg/mL	Nasopharyngeal carcinoma (CNE-1), rhinal epithelia, liver cancer (HepG2),	—	Greater photothermal therapeutic effect for larger number of internalized NPs per cells, under 0.2 W

TABLE 3 (Continued)

(C) in vitro and ex vivo studies

Study model	Laser setting				Nanoparticles		Injection mode	Concentration	Target	Temperature measurement method	Therapy outcome
	P (W) Pd (Wcm⁻²)	λ (nm)	t(s)		Type	Size (nm)					
					(FA), galactose (Gals))				liver normal cell types (L02), lymphosarcoma (8226), lymph normal cell types (H9)		laser irradiation, all the cells that had beyond 4.5×10^4 GNRs per cell died before 105 s, while such time for most cells that internalized GNRs less than 1.5×10^4 per cell was over 180 s.
Cell culture [61]	P: 0.04, 0.08 (Pd:10), 0.12, 0.16 (Pd:20), 0.2 (CW), laser beam spot size of 1 mm in diameter	800	240		GNR conjugated to anti-epidermal growth factor receptor (anti-EGFR) monoclonal antibodies	Aspect ratio: 3.9	Cells treated with NPs	—	Nonmalignant epithelial cell line (HaCat), Malignant oral epithelial cell lines (HOC 313 clone 8 and HSC 3)	—	$p \geq .16$, (Pd: 20) photodestruction of all HaCat cells; $p \geq .08$, (Pd: 10) malignant cells death in HOC 313 clones 8 and HSC 3.
Cell culture, Theoretical Model [58]	Pd: 20 (CW), laser beam spot size of 2 mm in diameter	800	240, 480, 720, 1200		GNRs@PEG	—	Cells treated with NPs	—	Human prostate cancer cell line (PC3-PSMA)	Thermocouple (Type J)	Extracellular hyperthermia generated by laser irradiation of NPs in the extracellular space.
	Pd: 20 (CW), laser beam spot size of 2 mm in diameter		900								Heat transport and cell death model consistent with experimental measurements.
Cell culture [156]	Pd:19, 25, 38, 50, 64, 76 (CW), laser beam spot size of 1 mm in diameter	514	240		Anti-epithelial growth factor receptor (EGFR) antibody conjugated GNSs	d: 40	Without NPs	0 mg/mL for control, 2 nM NP solution	Oral squamous carcinoma cell lines (HSC 313 and HOC 3 Clone 8) and one benign epithelial cell line (HaCaT)	—	Both cells required less than half the laser energy (25 and 19 W/cm²) to be killed than the benign cells (57 W/cm²) after incubation with anti-EGFR antibody conjugated NPs.
	Pd: 13, 19, 25, 32, 38, 45, 51, 57, 64 (CW),						Cells treated with NPs				

(Continues)

TABLE 3 (Continued)

(C) in vitro and ex vivo studies

Study model	Laser setting P (W) Pd (Wcm⁻²)	λ (nm)	t(s)	Nanoparticles Type	Size (nm)	Injection mode	Concentration	Target	Temperature measurement method	Therapy outcome
	laser beam spot size of 1 mm in diameter									
Cell culture [84]	Pd: 5.8 (CW), laser beam spot size ~2.7 mm	808	120-300	GNRs@PEG	W: 5 L: 25	Cells treated with NPs	2.5 nM	Human adenocarcinoma breast cancer cells (MCF-7)	33-gauge hypodermic thermocouple	For 2 min, 42.7% and 2.89%, whereas for 5 min 20.17% and 15.5% cell underwent apoptosis or necrosis, respectively.
Cell culture [287]	Pd: 20-90 (CW), laser beam spot size ~2.5 mm in diameter	808	60	GNRs@PEG conjugated to Anti-epithelial growth factor receptor (EGFR) antibody (anti-EGFR-GNRs)	—	Cells treated with NPs	~3 mM	EGFR expressing bladder cancer cells (HTB-9)	—	Cell death area for anti-EGFR-GNRs treated cells showed a sharp increase starting at 40 W/cm² and saturated at powers greater than 80 W/cm².
	Pd: 20 (CW), laser beam spot size ~2.5 mm in diameter		30-180							Cell death area showed a sharp increase between 1 and 2 min and saturated at longer exposure times.
Cell culture [283]	Pd: 32 (CW), laser beam spot size of 2 mm in diameter	808	180	Hollow GNSs@PEG attached with α-melanocyte stimulating hormone analog (NDP-MSH-PEG-HAuNS) and hollow GNSs@PEG	mean d of 43.5 ± 2.3 nm and mean shell thickness of 3 to 4 nm	Cells treated with NPs	3 × 10¹¹ particles/mL	Murine melanoma (B16/F10)	—	Histology shows significantly greater necrotic response with GNSs.
Cell culture [284]	Pd: 0.05 (CW), laser beam spot size of 30 mm in diameter	807	600	Gum Arabic-encapsulated GNPs (GA-GNPs)	d: 15-18	Cells treated with NPs	0.0016, 0.0024, 0.00374,0.0086 mg/mL	Human lung adenocarcinoma epithelial A549 cells	—	The exposure to laser irradiation for 10 min, after treating cells with different concentrations of GA-AuNPs, showed a

TABLE 3 (Continued)

(C) in vitro and ex vivo studies

Study model	Laser setting				Nanoparticles		Injection mode	Concentration	Target	Temperature measurement method	Therapy outcome
	P (W) Pd (Wcm⁻²)	λ (nm)	t(s)		Type	Size (nm)					
											significant gradual decrease in the cell viability to 65.4% with the highest used concentration (0.0086 mg/mL).
Ex vivo animal tissue [230]	P: 2.2 (CW)	808	10		Gold/copper polydopamine nanocomposite (Au/Cu@PDA NC)	—	NPs injected into blended tissue	—	Porcine pancreas tissue	Fiber Bragg grating sensors, Thermal Camera	The NC presence increased the maximum temperature reached during LA from 48°C (control) to 90°C (Au/Cu@PDA NC) at 2 mm, and from 33°C to 36°C at 4 mm distance from the laser tip.
Ex vivo animal tissue [257]	P: 1 (CW)	800	240		Gold/iron oxide NPs	d: 90	NPs injected into tissue	0.057 mg of gold/ mL	Fresh porcine muscle tissue	Photoacoustic and ultrasound imaging	Temperature elevation in the region with injected photoabsorbers slightly less than 10°C, while the surrounding region had a temperature rise less than 2°C. Maximum temperature difference less than 0.5°C, between the two imaging techniques.
Phantom, ex vivo animal tissue [4]	P: 0.5-2, Pd: 0.08, 0.16, 0.24, 0.32 (CW), beam width ~10 mm	806	1800		Silica/gold nanoshells (NSs) @PEG used in combination with Silver NSs	(core) d: ~120/ (shell) 15, d: 70 nm	Phantom loaded with NPs	0.0056 mg/mL	Agarose phantom	Thermal Camera	Temperature variation >5 K with 0.0056 mg/mL GNS and a laser power of 1.5 W.
					Silica/gold nanoshells (NSs) @PEG	(core) d: ~120/ (shell) 15	NPs injected into blended tissue	0.0058 mg/mL	Porcine cerebral tissues (stem,		The addition of plasmonic

(Continues)

TABLE 3 (Continued)

(C) in vitro and ex vivo studies

Study model	Laser setting				Nanoparticles				Target	Temperature measurement method	Therapy outcome
	P (W)	Pd (Wcm⁻²)	λ (nm)	t(s)	Type	Size (nm)	Concentration	Injection mode			
									cerebrum and cerebellum)		nanoparticles to the brain tissue increased the absorption coefficient of the whole sample and caused heating.

Abbreviations: CW, continuous wave; d, diameter; E, energy; F, fluence; f, frequency; fs, femtosecond; i.m., intramuscular; ip, intraperitoneal; i.t., intratumoral; i.v., intravenous; L, length; NR, nanorods; ns, nanosecond; NS, nanospheres; P, power; Pd, power density; PW, pulsed wave; Sub, subcutaneous; t, exposure time; Th, thickness; V, volume; W, width; λ, wavelength; τ, pulse width.

is the most mature approach for relative temperature measurement in tissues [242].

The good spatial and temporal resolution (eg, $1.25 \times 1.25 \times 3.5$ mm³, 1.9 seconds), together with the ability to accurately measure the temperature evolution in real-time and estimate the achieved thermal dose, makes MRI particularly suited for guiding thermal therapies [223, 243]. Because there is no interference of the laser with the MR scanner, PTT is well suited for MR-based thermal monitoring. Nevertheless, the dependence of thermal sensitivity on the type of tissue, the cost, the motion artifacts are some potential concerns [243]. Farashahi et al. have recently reported on the real-time monitoring of the heat generation and distribution in GNPs-loaded agar phantom irradiated by laser using MR-thermometry, in comparison with IR thermography (Figure 9B,C) [244]. Zabanran et al. have designed a study to investigate the effects of GNPs' characteristics (NPs' size, type, and concentration) and laser irradiation conditions on the thermal profile of an agar phantom during PTT. MR-based thermometry was used to validate the results obtained from simulation studies. They also suggested a protocol enabling the pre-clinical calculation and effect visualization for any NPs-based PTT procedure by having the optical properties of the NPs [245]. Both these studies show the MR-based thermometry potential in planning and monitoring the procedure in the presence of GNPs.

The dependence of several US parameters on temperature allows visualizing a temperature map, which is useful to adjust the laser dosimetry also in real-time [246, 247]. The affordability of US systems and the use of non-ionizing waves makes this technique appealing for clinical application, despite the motion artifacts and the unexpected variation in acoustic tissue properties. Regarding the use of the mentioned techniques in combination with NPs, several studies have proposed these imaging techniques for evaluating the multimodal contrast-capability of GNPs [248–250] and other materials [251].

The feasibility of CT-based thermometry during hyperthermal treatments has been reported since the 1970s [252–254]. However, a high patient dose of ionizing radiation is one of the main concerns related to this technique, together with dependence of the thermal sensitivity on the specific tissues, and the temporal resolution higher than 4 to 5 seconds [253, 255]. In association with GNPs, CT imaging is mostly used for therapy guidance rather than for thermometry. Indeed, GNPs have been widely employed as a contrast agent for CT imaging of different biological systems due to their enhanced X-ray attenuation property.

Photoacoustic imaging can be exploited to measure temperature by tracking the temperature induced

FIGURE 9 Image-based temperature measurements with (A) thermographic images of water medium with and without GNPs, MR thermometry in agar gel phantom (B) without GNPs, and (C) with GNPs [245]
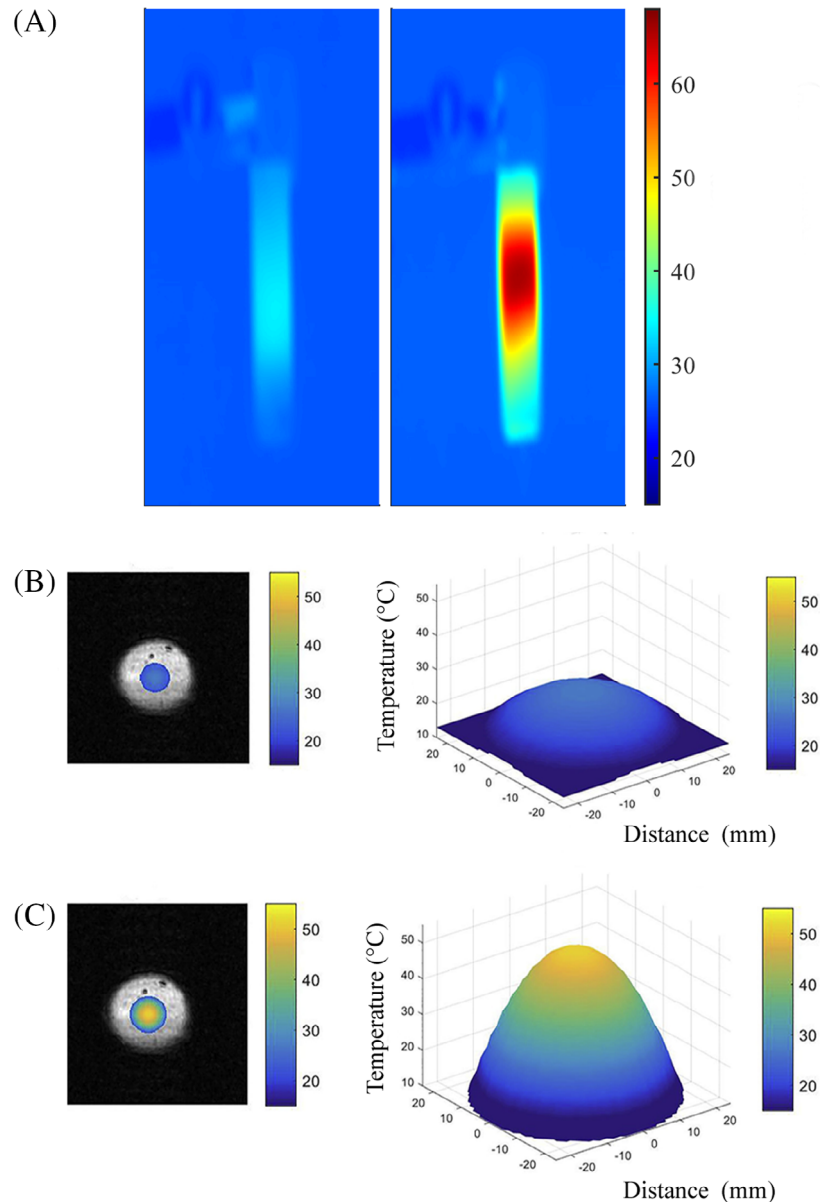
changes in photoacoustic signal amplitude based on the generation of pressure waves on the absorption of light energy [256]. A few works on the use of PA-thermometry during GNPs [257] and NPs-assisted PTT are available [258].

The imaging-based techniques here described are under the spotlight also for the optimization of the PTT guidance. In this regard, multifunctional nanoparticles are synthesized not only to increase the local tumor temperature by absorbing the NIR energy, but also to act as bimodal contrast agents. Theranostic agents have the ability to produce a signal detectable by the imaging systems, hence to allow the detection of the target in which they are deposited. Several agents have been developed for simple US imaging [259, 260], CT/X-ray imaging [261], or dual-modal imaging-guided PTT (eg, MRI/US,

PA/US) [262–265]; in combination with NIR conversion into heat, they hold great potential for PTT in cancer treatment.

6 | SIMULATIONS

Simulations are useful to pre-define the optimal settings for the specific treatment, as well as for investigating the influence of all the factors affecting the spatial distribution of heat in the tumor and healthy tissues, such as NPs' optical and thermal properties, their biodistribution within the tumor and biological tissues, and the adequate laser settings. As it was mentioned above, since both the cancerous and surrounding healthy cells absorb the laser radiation, damaging the nearby normal tissue is the main

risk of laser ablation. Thus, calculation of the temperature increase within the tumor and surrounding tissues guides the selection of the most promising combination of the laser settings and GNPs' properties [112, 236].

Several software packages are available to model thermal treatments in tissues [266]. To simulate a realistic electromagnetic-based thermal therapy for cancer, visualizer for electromagnetic dosimetry, and optimization (VEDO) software [267] has been designed [268, 269]. Field II Focus and k-wave are the softwares that are available for simulating the ultrasound-based hyperthermia planning.

Equation-based modeling for heat transfer and interaction between laser and medium is possible with the license based COMSOL Multiphysics software (http://www.comsol.com) in which the light propagation is modeled using the finite element method; therefore, the result precision and computing time depend on the grid size. In COMSOL, propagation of photons is described by diffusion approximation of the radiation transport equation, which is limited to systems where their absorption coefficients are lower than the reduced scattering. Diffusion approximation and propagation of light through a diffuse scattering medium with no absorption (Kubelka-Munk model) are based on hypotheses that are often not true for light scattering in tissues during phototherapy [270].

In the numerical study by Soni et al., the effect of the distribution of NPs delivered to skin tumor was investigate for the thermal ablation condition attained during thermal therapy. In this work, they used three distributions for NPs, and they highlighted the role of NPs distribution on the spatiotemporal temperature fields within a two-dimensional skin tumor. By this numerical work, they made a framework to incorporate distribution of GNRs in the numerical models, which is achievable in practice, thus giving prediction of temperature toward pretreatment [271].

Rossi et al. used COMSOL Multiphysics software to indicate the laser irradiation-related parameters in the design of a new approach based on the use of GNRs in the hyperthermia of tumor. This model aims at designing the correct settings of the laser to induce effective temperature values in the biological tissue, avoiding to induce thermal damage at the nanoscale level to the GNRs [272]. This multi-physical field software can be utilized to couple the light and heat physical fields and used for defining scattering cross-section and laser-induced heat at the single nanoparticle level and for increasingly more complex modeling which can exploit Monte Carlo method and bioheat equation [273]. It can be used also in combination with 3D image processing and model generation software for complex PTT and interstitial PTT scheme [274, 275].

In another simulation study by Gheflati et al., COMSOL Multiphysics software was used to investigate the optimum laser intensity for laser-induced hyperthermia with the assistance of nonuniform-distributed GNRs within the tumor. They utilized the periodic heating method to solve the problem of surface overheating and apply such an optimum intensity. The results showed that such a model can optimize the laser power while minimizing the surface overheating problem [276].

Shurrab et al. developed a mathematical model of temperature distribution and light propagating in the tissue during laser-induced hyperthermia to study the effective laser-related parameters to control hyperthermia. They used COMSOL to simulate the light diffusion and bioheat equation in a mouse model as well as the effect of different parameters like power and irradiation exposure time on the tumor surrounding tissues with the aim of decreasing detrimental effects [277].

Mooney and colleagues have also implemented a finite element model on COMSOL Multiphysics, simulating GNRs-enhanced laser therapy in mice, and comparing these results with experimental data [48].

The Geant4 Application for Emission Tomography (GATE) open-source simulation platform, based on the Geant4 toolkit, has been developed since 2001 by the OpenGATE collaboration [278–281]. This software has been currently widely used by the research community involved in molecular imaging, radiotherapy, and optical imaging.

To enable modeling of NPs-mediated hyperthermia therapy and simplify the heat diffusion in biological tissues, Cuplov et al. have presented an extension of this software [282]. Such a new feature of GATE combined with optical imaging has made it possible to simulate a theranostic scenario in which the patient is injected with theranostic nanosystems and can be simultaneously treated with both the therapeutic and fluorescence imaging agents. This study demonstrated that NPs-mediated NIR thermal therapy could be accurately simulated with GATE and reproduce experimental data.

7 | DISCUSSION AND CONCLUSIVE OUTLOOK

Since their introduction in the 1960s, minimally invasive thermal treatments have gained large interest for the management of solid tumors. Among them, PTT stands out as a promising procedure, relying on the conversion of the light absorbed by biological tissue into heat in synergy with a highly-absorbing photosensitizer. At present, combinational therapy, based on different modalities like such a technique, mediated by nanotechnology, has been

the trend in pre-clinical and clinical research and, recently, in a clinical scenario [43].

Even though the literature of this field is solid and daily enriched, a broad overview of the main physical, chemical, biological aspects at the practical bases of the GNPs-assisted PTT is still indispensable to get oriented in such a complex topic.

Table 3 summarizes several significant studies, to point out the main procedural settings and the resulting thermal outcome. Different factors such as size, shape, concentration, coating, and modification of the surface, as well as the route of injection, influence the NPs targeting and accumulation in tissues, also affecting the overall photothermal heating efficiency (Figure 10).

The most used wavelength values for the laser source have resulted to be the range 520 to 550 nm for GNSs [156, 244, 245] and 800 to 810 nm in combination with GNRs with correspondent longitudinal surface plasmon resonance peak [58,84,117,237,283,284]. Of these ranges, 800 nm is preferred because included within the therapeutic window and producing a lower absorption within healthy tissue with respect to 500 to 600 nm, which is dominated by the absorption of the oxyhemoglobin.

Laser power values have revealed to be highly study dependent. Indeed, the laser energy is delivered continuously (CW), or, more rarely, in pulsed (PW) modality. Furthermore, the power (P) is often defined in terms of power density (Pd, ie, the ratio between the power and the laser spot area), underlining also the influence of the

beam spot in the energy deposition inside the biological medium. After clustering all this various information, it emerges that the laser energy is mostly delivered in CW. Although Pd and the laser beam characteristics are selected according to the desired thermal effect on the target, therefore they vary depending upon each experimental design, some typical ranges can be identified among preclinical studies. Regarding in vivo investigations, Pd values ranging from 0.5 W/cm^2 to approximately 6 W/cm^2 can be observed, as well as 2.7 to 30 mm beam spot sizes [53,84,112,117,236,237,239,240,259,283,284]. Whereas, Pd of 0.05 to 90 W/cm^2, and beam focal spots comprised between 2 and 30 mm in diameter are employed in in vitro scenarios [58,61,84,156,244,245,283–287].

The heterogeneity of these parameters impairs a straight comparison of the studies in terms of the outcome. The large variety of this setting is an index of the current status of the research, which is still working on the identification of the suitable ranges for the specific target. The PW modality is, instead, largely used to evaluate the effects of the irradiation on the change of morphology of the GNRs (Table 2).

Regarding the irradiation time, treatments have a typical duration of 30 to 600 seconds in most of the in vivo studies [237, 239, 244, 245, 286], with some exception concerning in vitro experiments which can last until 1200 seconds [58].

The in vivo experiments for the assessment of the therapy outcome are usually conducted in mice, whereas

FIGURE 10 Different factors and their interplay on the thermal outcome in GNPs-mediated PTT. Gold nanoparticles (GNPs) are unique therapeutic agents for minimally invasive photothermal therapy of cancer. Several GNPs parameters, for example, optical properties, coating, and concentration, in association with laser settings and tumor properties, significantly impact therapy outcomes. Understanding the physical mechanisms for heat generation in GNPs-embedded tissues is fundamental for the design of experiments and planning and monitoring tools, toward the therapy settings optimization for the final clinical application
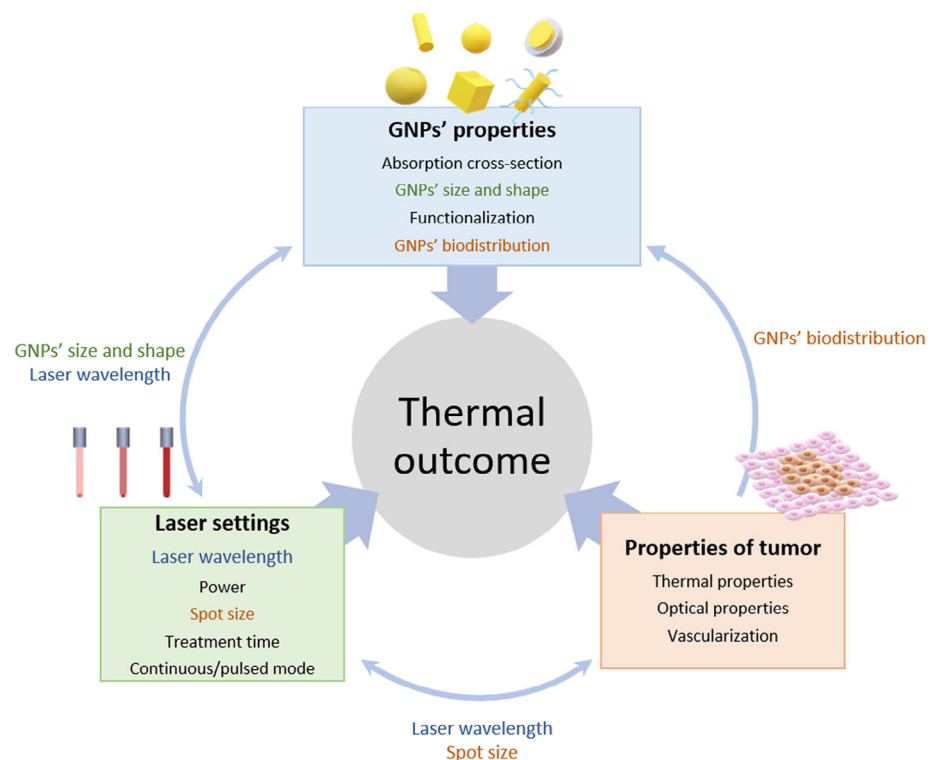
some agar-phantom experiments have been carried out to assess the thermal efficacy of the GNPs, varying the procedure settings (eg, irradiation time and power). Several GNPs' concentrations have been assessed, ranging from 0.005 to 0.2 mg/mL [236, 239, 244, 287], and both i.v. and intratumoral (i.t.) injection routes are used in animal model studies. The injection modality has proved to influence both the therapy outcome and the biodistribution: indeed, i.v. and intraperitoneal (i.p.) cause accumulation of GNPs mostly in liver and spleen after 24 hours [83,119], whereas oral administration revealed prominent accumulation in the kidney [74] (Table 1). The pilot studies in patients with prostate cancer used i.v. injection, with a dose of 7.5 mL/kg, including around 100 OD gold-silica nanoshells, corresponding to ~2.77 $\times 10^{11}$ particles/mL [43,55].

Moving from the settings to the outcome evaluation, change in the morphology (Table 2), toxicity, and pharmacokinetics of NPs should also be considered while assessing the long-term behavior of the nanostructures within the biological structures. A further concern is the evaluation of the thermal tissue damage and the necessity to monitor the thermal effect of the procedure. Temperature values above 50°C induced by 808 nm laser at 3 W (CW) for at least 3 minutes have shown therapeutically efficacy in murine models (colon carcinoma and human breast cancer cells) [117, 236]. It is worth underlining that temperature is one of the most accessible physiological parameters to be monitored during the procedure. Indeed, the tissue temperature is the direct evaluation of the effects of the ongoing therapy and is related to the desired cells heat-induced damage. As observable from Table 3, only a part of the studies minds about thermometry. A subgroup uses single probes (eg, thermocouples) [53,58,84,117,236], whereas the others perform MR thermometry of thermography for obtaining information about the temperature distribution inside and around the target organ [237, 239 244, 245, 286].

Intraprocedural temperature information could help in tuning the laser settings (power and time). Alternatively, some works have based their settings choice on the prediction provided by theoretical models. The development of reliable simulation-based tools represents another key factor for the optimization of GNRs-assisted photothermal treatments. Theoretical and computational studies based on finite element methods and Monte Carlo-based tools have demonstrated to estimate with sufficient accuracy the temperature values reached in tissues undergoing irradiations [214]. The accurate prediction on the spatial temperature evolutions proved to be mostly influenced by the optical, mechanical and thermal properties of tissue and GNPs properties [23,271,276]. The availability of simulation-based tools is crucial to foresee the tissue thermal damage, thus, to guide the design of experimental studies and to evaluate a priori the temperature outcome.

Nevertheless, further studies are needed for the establishment of simulations considering the real tumor and biological off-target tissue geometries, and the correct estimation of tissue properties and metabolic-related processes, such as perfusion and vascularization contributions. Thus, despite holding great potential and peculiar features, concerns such as the unknown long-term cytotoxicity, still limit the widespread transitioning of a safe photothermal technique to the clinical stages. Future investigations should focus on the implementation of a standardized intervention procedure and the synergetic application of nanotechnologies approaches, real-time temperature measurement methods, and treatment simulation systems for bridging GNRs-assisted laser PTT into clinical scenarios.

DATA AVAILABILITY STATEMENT

Data sharing is not applicable to this article as no new data were created in this study.

AUTHOR BIOGRAPHIES

Please see Supporting Information online.

ORCID

Somayeh Asadi https://orcid.org/0000-0002-7118-1772

REFERENCES

[1] E. Schena, P. Saccomandi, Y. Fong, *J. Funct. Biomater.* **2017**, *8*, 19.

[2] M. Ahmed, C. L. Brace, F. T. Lee, S. N. Goldberg, *Radiology* **2011**, *258*, 351.

[3] J. Pearce, *Int. J. Hyperthermia* **2011**, *27*, 741.

[4] Y. He, K. Laugesen, D. Kamp, S. A. Sultan, L. B. Oddershede, L. Jauffred, *Cancer Nanotechnol.* **2019**, *10*, 8.

[5] X. Huang, M. A. El-Sayed, *Alexandria J. Med.* **2011**, *47*, 1.

[6] J. B. Vines, J. H. Yoon, N. E. Ryu, D. J. Lim, H. Park, *Front. Chem.* **2019**, *7*, 167.

[7] D. Jaque, L. Martínez Maestro, B. Del Rosal, P. Haro-Gonzalez, A. Benayas, J. L. Plaza, E. Martín Rodríguez, J. García Solé, *Nanoscale* **2014**, *6*, 9494.

[8] R. J. Stafford, D. Fuentes, A. A. Elliott, J. S. Weinberg, K. Ahrar, *Crit. Rev. Biomed. Eng.* **2010**, *38*, 79.

[9] G. Eskiizmir, Y. Baskın, K. Yapıcı, Graphene-based nanomaterials in cancer treatment and diagnosis. in *Fullerens, Graphenes and Nanotubes* (Ed: A. Grumezescu), Elsevier, Amsterdam **2018**, p. 331.

[10] T. M. Liu, J. Conde, T. Lipiński, A. Bednarkiewicz, C. C. Huang, *NPG Asia Mater.* **2016**, *8*, e295.

[11] B. Jang, J. Y. Park, C. H. Tung, I. H. Kim, Y. Choi, *ACS Nano* **2011**, *5*, 1086.

[12] A. J. McGrath, Y. H. Chien, S. Cheong, D. A. J. Herman, J. Watt, A. M. Henning, L. Gloag, C. S. Yeh, R. D. Tilley, *ACS Nano* **2015**, *9*, 12283.

[13] K. Yang, L. Hu, X. Ma, S. Ye, L. Cheng, X. Shi, C. Li, Y. Li, Z. Liu, *Adv. Mater.* **2012**, *24*, 1868.

[14] X. Wang, C. Wang, L. Cheng, S. T. Lee, Z. Liu, *J. Am. Chem. Soc.* **2012**, *134*, 7414.

[15] W. Miao, G. Shim, S. Lee, Y. K. Oh, *Biomaterials* **2014**, *35*, 4058.

[16] L. Cheng, K. Yang, Q. Chen, Z. Liu, *ACS Nano* **2012**, *6*, 5605.

[17] D. K. Ledezma, P. B. Balakrishnan, J. Cano-Mejia, E. E. Sweeney, M. Hadley, C. M. Bollard, A. Villagra, R. Fernandes, *Nanomaterials* **2020**, *10*.

[18] C. Liu, S. Zhang, J. Li, J. Wei, K. Müllen, M. Yin, *Angew. Chem. Int. Ed.* **2019**, *58*, 1638.

[19] Y. Xu, Y. Zhang, X. Cai, W. Gao, X. Tang, Y. Chen, J. Chen, L. Chen, Q. Tian, S. Yang, Y. Zheng, B. Hu, *Int. J. Nanomedicine* **2019**, *14*, 271.

[20] M. Gautam, K. Poudel, C. S. Yong, J. O. Kim, *Int. J. Pharm.* **2018**, *549*, 31.

[21] D. Cassano, M. Santi, F. D'Autilia, A. K. Mapanao, S. Luin, V. Voliani, *Mater. Horizons.* **2019**, *6*, 531.

[22] V. Shanmugam, S. Selvakumar, C. S. Yeh, *Chem. Soc. Rev.* **2014**, *43*, 6254.

[23] L. R. Hirsch, R. J. Stafford, J. A. Bankson, S. R. Sershen, B. Rivera, R. E. Price, J. D. Hazle, N. J. Halas, J. L. West, *Proc. Natl. Acad. Sci. U. S. A.* **2003**, *100*, 13549.

[24] X. He, X. Bao, H. Cao, Z. Zhang, Q. Yin, W. Gu, L. Chen, H. Yu, Y. Li, *Adv. Funct. Mater.* **2015**, *25*, 2831.

[25] D. Wang, Z. Xu, H. Yu, X. Chen, B. Feng, Z. Cui, B. Lin, Q. Yin, Z. Zhang, C. Chen, J. Wang, W. Zhang, Y. Li, *Biomaterials* **2014**, *35*, 8374.

[26] F. Zhou, X. Li, M. F. Naylor, T. Hode, R. E. Nordquist, L. Alleruzzo, J. Raker, S. S. K. Lam, N. Du, L. Shi, X. Wang, W. R. Chen, *Cancer Lett.* **2015**, *359*, 169.

[27] Q. Chen, C. Liang, C. Wang, L. Zhuang, *Adv. Mater.* **2015**, *27*, 903.

[28] Z. Zhang, J. Wang, X. Nie, T. Wen, Y. Ji, X. Wu, Y. Zhao, C. Chen, *J. Am. Chem. Soc.* **2014**, *136*, 7317.

[29] T. Okuno, S. Kato, Y. Hatakeyama, J. Okajima, S. Maruyama, M. Sakamoto, S. Mori, T. Kodama, *J. Control. Release* **2013**, *172*, 879.

[30] L. Wang, X. Lin, J. Wang, Z. Hu, Y. Ji, S. Hou, Y. Zhao, X. Wu, C. Chen, *Adv. Funct. Mater.* **2014**, *24*, 4229.

[31] S. Parida, C. Maiti, Y. Rajesh, K. K. Dey, I. Pal, A. Parekh, R. Patra, D. Dhara, P. K. Dutta, M. Mandal, *Biochim. Biophys. Acta - Gen. Subj.* **2017**, *1861*, 3039.

[32] X. Huang, F. Xu, H. Hou, J. Hou, Y. Wang, S. Zhou, *Nano Res.* **2019**, *12*, 1361.

[33] M. Khafaji, M. Zamani, M. Golizadeh, O. Bavi, *Biophys. Rev.* **2019**, 1.

[34] J. Nam, S. Son, L. J. Ochyl, R. Kuai, A. Schwendeman, J. J. Moon, *Nat. Commun.* **2018**, *9*, 1.

[35] Z. Zhang, J. Wang, C. Chen, *Adv. Mater.* **2013**, *25*, 3869.

[36] A. Zhang, A. Li, W. Zhao, J. Liu, *Chem. Eur. J.* **2018**, *24*, 4215.

[37] Z. Huang, L. Kong, L. Gao, H. H. Zhang, J. X. Yang, L. Li, *J. Mater. Chem. B* **2019**, *7*, 7377.

[38] W. Ngwa, H. Korideck, A. I. Kassis, R. Kumar, S. Sridhar, G. M. Makrigiorgos, R. A. Cormack, *Nanomed. Nanotechnol. Biol. Med.* **2013**, *9*, 25.

[39] A. O. Govorov, H. H. Richardson, *Nano Today.* **2007**, *2*, 30.

[40] M. R. Kanavi, S. Asadi, S. Balagholi, F. Alikarami, H. Nosrati, H. Ahmadieh, *J. Appl. Clin. Med. Phys.* **2018**, *19*, 268.

[41] P. Tiwari, K. Vig, V. Dennis, S. Singh, *Nanomaterials* **2011**, *1*, 31.

[42] Y. Fu, Q. Feng, Y. Shen, M. Chen, C. Xu, Y. Cheng, X. Zhou, *RSC Adv.* **2018**, *8*, 6120.

[43] A. R. Rastinehad, H. Anastos, E. Wajswol, J. S. Winoker, J. P. Sfakianos, S. K. Doppalapudi, M. R. Carrick, C. J. Knauer, B. Taouli, S. C. Lewis, A. K. Tewari, J. A. Schwartz, S. E. Canfield, A. K. George, J. L. West, N. J. Halas, *Proc. Natl. Acad. Sci. U. S. A.* **2019**, *116*, 18590.

[44] J. F. Dorsey, L. Sun, D. Y. Joh, A. Witztum, G. D. Kao, M. Alonso-Basanta, S. Avery, S. M. Hahn, A. Al Zaki, A. Tsourkas, *Transl. Cancer Res.* **2013**, *2*, 280.

[45] D. Xi, S. Dong, X. Meng, Q. Lu, L. Meng, J. Ye, *RSC Adv.* **2012**, *2*, 12515.

[46] T. Reuveni, M. Motiei, Z. Romman, A. Popovtzer, R. Popovtzer, *Int. J. Nanomedicine* **2011**, *6*, 2859.

[47] T. Ahmad, R. Sarwar, A. Iqbal, U. Bashir, U. Farooq, S. A. Halim, A. Khan, A. Al-Harrasi, *Nanomedicine* **2020**.

[48] N. S. Abadeer, C. J. Murphy, *J. Phys. Chem. C* **2016**, *120*, 4691.

[49] S. Link, M. A. El-Sayed, *Annu. Rev. Phys. Chem.* **2003**, *54*, 331.

[50] H.-C. Huang, S. Barua, D. B. Kay, K. Rege, *ACS Nano* **2009**, *3*, 2941.

[51] X. Huang, S. Neretina, M. A. El-Sayed, *Adv. Mater.* **2009**, *21*, 4880.

[52] S. Link, M. A. El-Sayed, *Int. Rev. Phys. Chem.* **2000**, *19*, 409.

[53] E. B. Dickerson, E. C. Dreaden, X. Huang, I. H. El-Sayed, H. Chu, S. Pushpanketh, J. F. McDonald, M. A. El-Sayed, *Cancer Lett.* **2008**, *269*, 57.

[54] A. Iglic, M. Rappolt, A. Garcia-Saez, *Advances in Biomembranes and Lipid Self-Assembly*, Vol. 27, Academic Press, New York **2018**.

[55] J. M. Stern, V. V. Kibanov Solomonov, E. Sazykina, J. A. Schwartz, S. C. Gad, G. P. Goodrich, *Int. J. Toxicol.* **2016**, *35*, 38.

[56] N. Manuchehrabadi, L. Zhu, *Handb. Therm. Sci. Eng.* **2017**, 1.

[57] A. N. Yakunin, S. V. Zarkov, Y. A. Avetisyan, G. G. Akchurin, G. G. Akchurin Jr, E. S. Tuchina, V. V. Tuchin (**2019**) Modeling of hyperthermia induced by functionalized gold nanorods bound to *Staphylococcus aureus* under NIR laser radiation. Paper presented at: Proceedings Volume 11065, Saratov Fall Meeting 2018: Optical and Nano-Technologies for Biology and Medicine; 1106516. https://doi.org/10.1117/12.2531440.

[58] H.-C. Huang, K. Rege, J. J. Heys, *ACS Nano* **2010**, *4*, 2892.

[59] H. J. Moon, M. Ku, H. Lee, N. Yoon, J. Yang, K. W. Bong, *Sci. Rep.* **2018**, *8*, 13683.

[60] B. Jang, Y. S. Kim, Y. Choi, *Small* **2011**, *7*, 265.

[61] X. Huang, I. H. El-Sayed, W. Qian, M. A. El-Sayed, *J. Am. Chem. Soc.* **2006**, *128*, 2115.

[62] S. R. Bhattarai, P. J. Derry, K. Aziz, P. K. Singh, A. M. Khoo, A. S. Chadha, A. Liopo, E. R. Zubarev, S. Krishnan, *Nanoscale* **2017**, *9*, 5085.

[63] R. Toy, P. M. Peiris, K. B. Ghaghada, E. Karathanasis, *Nanomedicine* **2014**, *9*, 121.

[64] A. G. Tkachenko, H. Xie, Y. Liu, D. Coleman, J. Ryan, W. R. Glomm, M. K. Shipton, S. Franzen, D. L. Feldheim, *Bioconjug. Chem.* **2004**, *15*, 482.

[65] J. Zhou, J. Ralston, R. Sedev, D. A. Beattie, *J. Colloid Interface Sci.* **2009**, *331*, 251.

[66] S. Takae, Y. Akiyama, H. Otsuka, T. Nakamura, Y. Nagasaki, K. Kataoka, *Biomacromolecules* **2005**, *6*, 818.

[67] B. Du, Z. Li, Y. Cheng, *Talanta* **2008**, *75*, 959.

[68] M. Jedrzejczak-Silicka, E. Mijowska, General Cytotoxity and Its Application in Nanomaterial Analysis. in *Cytotoxicity* (Ed: T. A. Çelik), IntechOpen, Croatia **2018**.

[69] D. Chenthamara, S. Subramaniam, S. G. Ramakrishnan, S. Krishnaswamy, M. M. Essa, F. H. Lin, M. W. Qoronfleh, *Biomater. Res.* **2019**, *23*, 1.

[70] M. Bednarski, M. Dudek, J. Knutelska, L. Nowiński, J. Sapa, M. Zygmunt, G. Nowak, M. Luty-Błocho, M. Wojnicki, K. Fitzner, M. Tęsiorowski, *Pharmacol. Rep.* **2015**, *67*, 405.

[71] M. Wojnicki, M. Luty-Blocho, M. Bednarski, M. Dudek, J. Knutelska, J. Sapa, M. Zygmunt, G. Nowak, K. Fitzner, *Pharmacol. Rep.* **2013**, *65*, 1033.

[72] L. Yang, H. Kuang, W. Zhang, Z. P. Aguilar, H. Wei, H. Xu, *Sci. Rep.* **2017**, *7*.

[73] G. Sonavane, K. Tomoda, K. Makino, *Colloids Surf. B Biointerfaces* **2008**, *66*, 274.

[74] J. F. Hillyer, R. M. Albrecht, *J. Pharm. Sci.* **2001**, *90*, 1927.

[75] J. F. Hainfeld, F. A. Dilmanian, D. N. Slatkin, H. M. Smilowitz, *J. Pharm. Pharmacol.* **2008**, *60*, 977.

[76] L. Yao, J. Daniels, A. Moshnikova, S. Kuznetsov, A. Ahmed, D. M. Engelman, Y. K. Reshetnyak, O. A. Andreev, *Proc. Natl. Acad. Sci. U. S. A.* **2013**, *110*, 465.

[77] N. Chen, W. Yang, Y. Bao, H. Xu, S. Qin, Y. Tu, *RSC Adv.* **2015**, *5*, 40514.

[78] S. Jain, J. A. Coulter, A. R. Hounsell, K. T. Butterworth, S. J. McMahon, W. B. Hyland, M. F. Muir, G. R. Dickson, K. M. Prise, F. J. Currell, *Int. J. Radiat. Oncol. Biol. Phys.* **2011**, *79*, 531.

[79] S.-D. Li, L. Huang, *Mol. Pharm.* **2008**, *5*, 496.

[80] M. J. Ernsting, M. Murakami, A. Roy, S. D. Li, *J. Control. Release* **2013**, *172*, 782.

[81] N. Khlebtsov, L. Dykman, *Chem. Soc. Rev.* **2011**, *40*, 1647.

[82] W. H. De Jong, W. I. Hagens, P. Krystek, M. C. Burger, A. J. A. M. Sips, R. E. Geertsma, *Biomaterials* **2008**, *29*, 1912.

[83] M. R. K. Ali, M. A. Rahman, Y. Wu, T. Han, X. Peng, M. A. Mackey, D. Wang, H. J. Shin, Z. G. Chen, H. Xiao, R. Wu, Y. Tang, D. M. Shin, M. A. El-Sayed, *Proc. Natl. Acad. Sci. U. S. A.* **2017**, *114*, E3110.

[84] M. A. El-Sayed, M. Ali, I. Ibrahim, H. Ali, S. Selim, *Int. J. Nanomedicine* **2016**, *11*, 4849.

[85] M. R. Kanavi, S. Asadi, H. Ahmadieh, *Int. J. Nanomedicine* **2017**, *12*, 8527.

[86] D. Sahu, G. M. Kannan, M. Tailang, R. Vijayaraghavan, *J. Nanosci.* **2016**, *2016*, 1.

[87] S. Park, Y. K. Lee, M. Jung, K. H. Kim, N. Chung, E. K. Ahn, Y. Lim, K. H. Lee, *Inhal. Toxicol.* **2007**, *19*, 59.

[88] A. Ivask, T. Titma, M. Visnapuu, H. Vija, A. Kakinen, M. Sihtmae, S. Pokhrel, L. Madler, M. Heinlaan, V. Kisand, R. Shimmo, A. Kahru, *Curr. Top. Med. Chem.* **2015**, *15*, 1914.

[89] I. Fratoddi, I. Venditti, C. Cametti, M. V. Russo, *Nano Res.* **2015**, *8*, 1771.

[90] N. Lewinski, V. Colvin, R. Drezek, *Small* **2008**, *4*, 26.

[91] B. Kong, J. H. Seog, L. M. Graham, S. B. Lee, *Nanomedicine* **2011**, *6*, 929.

[92] H. Bahadar, F. Maqbool, K. Niaz, M. Abdollahi, *Iran. Biomed. J.* **2016**, *20*, 1.

[93] E. Boisselier, D. Astruc, *Chem. Soc. Rev.* **2009**, *38*, 1759.

[94] C. M. Goodman, C. D. McCusker, T. Yilmaz, V. M. Rotello, *Bioconjug. Chem.* **2004**, *15*, 897.

[95] H. K. Patra, S. Banerjee, U. Chaudhuri, P. Lahiri, A. K. Dasgupta, *Nanomed. Nanotechnol. Biol. Med.* **2007**, *3*, 111.

[96] A. Woźniak, A. Malankowska, G. Nowaczyk, B. F. Grześkowiak, K. Tuśnio, R. Słomski, A. Zaleska-Medynska, S. Jurga, *J. Mater. Sci. Mater. Med.* **2017**, *28*, 92.

[97] H. Cai, P. Yao, *Colloids Surf. B Biointerfaces* **2014**, *123*, 900.

[98] M. A. Vetten, N. Tlotleng, D. Tanner Rascher, A. Skepu, F. K. Keter, K. Boodhia, L. A. Koekemoer, C. Andraos, R. Tshikhudo, M. Gulumian, *Part. Fibre Toxicol.* **2013**, *10*, 50.

[99] B. Yahyaei, M. Nouri, S. Bakherad, M. Hassani, P. Pourali, *AMB Express.* **2019**, *9*, 38.

[100] E. E. Connor, J. Mwamuka, A. Gole, C. J. Murphy, M. D. Wyatt, *Small* **2005**, *1*, 325.

[101] H. Sun, J. Jia, C. Jiang, S. Zhai, *Int. J. Mol. Sci.* **2018**, *19*, 754.

[102] M. A. Arnida, A. Malugin, H. Ghandehari, *J. Appl. Toxicol.* **2010**, *30*, 212.

[103] A. M. Alkilany, P. K. Nagaria, C. R. Hexel, T. J. Shaw, C. J. Murphy, M. D. Wyatt, *Small* **2009**, *5*, 701.

[104] C. Carnovale, G. Bryant, R. Shukla, V. Bansal, *ACS Omega* **2019**, *4*, 242.

[105] Y. Qu, X. Lü, *Biomed. Mater.* **2009**, *4*.

[106] C. Brandenberger, B. Rothen-Rutishauser, C. Mühlfeld, O. Schmid, G. A. Ferron, K. L. Maier, P. Gehr, A. G. Lenz, *Toxicol. Appl. Pharmacol.* **2010**, *242*, 56.

[107] Y. Pan, A. Leifert, D. Ruau, S. Neuss, J. Bornemann, G. Schmid, W. Brandau, U. Simon, W. Jahnen-Dechent, *Small* **2009**, *5*, 2067.

[108] K. D. Sattler, *Handbook of nanophysics: Functional nanomaterials*, Routledge, London **2010**.

[109] Y. Pan, S. Neuss, A. Leifert, M. Fischler, F. Wen, U. Simon, G. Schmid, W. Brandau, W. Jahnen-Dechent, *Small* **2007**, *3*, 1941.

[110] M. R. K. Ali, Y. Wu, M. A. El-Sayed, *J. Phys. Chem. C* **2019**, *123*, 15375.

[111] X. M. Zhu, C. Fang, H. Jia, Y. Huang, C. H. K. Cheng, C. H. Ko, Z. Chen, J. Wang, Y. X. J. Wang, *Nanoscale* **2014**, *6*, 11462.

[112] R. Mooney, E. Schena, P. Saccomandi, A. Zhumkhawala, K. Aboody, J. M. Berlin, *Int. J. Hyperthermia* **2017**, *33*, 150.

[113] J. F. Liao, W. T. Li, J. R. Peng, Q. Yang, H. Li, Y. Q. Wei, X. N. Zhang, Z. Y. Qian, *Theranostics* **2015**, *5*, 345.

[114] E. J. Moding, M. B. Kastan, D. G. Kirsch, *Nat. Rev. Drug Discov.* **2013**, *12*, 526.

[115] W. T. Phillips, A. Bao, A. J. Brenner, B. A. Goins, *Adv. Drug Deliv. Rev.* **2014**, *76*, 39.

[116] O. B. Adewale, H. Davids, L. Cairncross, S. Roux, *Int. J. Toxicol.* **2019**, *38*, 357.

[117] G. P. Goodrich, L. Bao, K. Gill-Sharp, K. L. Sang, J. Wang, J. D. Payne, *J. Biomed. Opt.* **2010**, *15*, 018001.

[118] V. Khare, N. Alam, A. Saneja, R. D. Dubey, P. N. Gupta, *J. Biomed. Nanotechnol.* **2014**, *10*, 3462.

[119] R. R. Arvizo, O. R. Miranda, D. F. Moyano, C. A. Walden, K. Giri, R. Bhattacharya, J. D. Robertson, V. M. Rotello, J. M. Reid, P. Mukherjee, *PLoS One* **2011**, *6*, e24374.

[120] S. K. Mouli, P. Tyler, J. L. McDevitt, A. C. Eifler, Y. Guo, J. Nicolai, R. J. Lewandowski, W. Li, D. Procissi, R. K. Ryu, *ACS Nano* **2013**, *7*, 7724.

[121] K. Sano, T. Nakajima, P. L. Choyke, H. Kobayashi, *ACS Nano* **2013**, *7*, 717.

[122] E. Blanco, H. Shen, M. Ferrari, *Nat. Biotechnol.* **2015**, *33*, 941.

[123] Q. Sun, Z. Zhou, N. Qiu, Y. Shen, *Adv. Mater.* **2017**, *29*, 1606628.

[124] J.-X. Li, Q.-Y. Huang, J.-Y. Zhang, J. Du, *J. Mater. Chem. B* **2020**.

[125] Y.-F. Zhou, *World J. Clin. Oncol.* **2011**, *2*, 8.

[126] R. A. Baum, S. Baum, *Radiology* **2014**, *273*, S75.

[127] J. Li, F. Liu, S. Gupta, C. Li, *Theranostics* **2016**, *6*, 1393.

[128] R. A. Petros, J. M. DeSimone, *Nat. Rev. Drug Discov.* **2010**, *9*, 615.

[129] J. Shi, A. R. Votruba, O. C. Farokhzad, R. Langer, *Nano Lett.* **2010**, *10*, 3223.

[130] D. A. Giljohann, D. S. Seferos, W. L. Daniel, M. D. Massich, P. C. Patel, C. A. Mirkin, *Angew. Chem. Int. Ed.* **2010**, *49*, 3280.

[131] J. B. Delehanty, K. Boeneman, C. E. Bradburne, K. Robertson, J. E. Bongard, I. L. Medintz, *Ther. Deliv.* **2010**, *1*, 411.

[132] R. Chouaib, R. Sarieddine, H. Gali-Muhtasib, Nanoparticles as Drug Delivery Systems for Cancer Treatment: Applications in Targeted Therapy and Personalized Medicine. in *Nanoparticle Drug Delivery Systems for Cancer Treatment* (Eds: H. Gali-Muhtasib, R. Chouaib), Taylor & Francis, London **2020**, p. 1.

[133] A. Friedman, S. Claypool, R. Liu, *Curr. Pharm. Des.* **2013**, *19*, 6315.

[134] Y. H. Cheng, C. He, J. E. Riviere, N. A. Monteiro-Riviere, Z. Lin, *ACS Nano* **2020**, *14*, 3075.

[135] X. Huang, X. Peng, Y. Wang, Y. Wang, D. M. Shin, M. A. El-Sayed, S. Nie, *ACS Nano* **2010**, *4*, 5887.

[136] L. A. Dykman, N. G. Khlebtsov, *Acta Nat.* **2011**, *3*, 34.

[137] F. Benyettou, A. Ramdas Nair, Y. Dho, T. Prakasam, R. Pasricha, J. Whelan, H. Traboulsi, J. Mazher, K. C. Sadler, A. Trabolsi, *Chem. Eur. J.* **2020**, *26*, 5270.

[138] C. Oliveira, A. J. Ribeiro, F. Veiga, I. Silveira, *J. Biomed. Nanotechnol.* **2016**, *12*, 841.

[139] Y. Xiao, K. Shi, Y. Qu, B. Chu, Z. Qian, *Mol. Ther. - Methods Clin. Dev.* **2019**, *12*, 1.

[140] D.-W. Han, T. S. Atabaev, *The Two Faces of Nanomaterials: Toxicity and Bioactivity*, Multidisciplinary Digital Publishing InstituteMDPI, Basel, Switzerland **2020**.

[141] M. Bekić, S. Tomić, R. Rudolf, M. Milanović, D. Vučević, I. Anžel, M. Čolić, *Materials (Basel)* **2019**, *12*, 4121.

[142] A. Espinosa, A. Curcio, S. Cabana, G. Radtke, M. Bugnet, J. Kolosnjaj-Tabi, C. Péchoux, C. Alvarez-Lorenzo, G. A. Botton, A. K. A. Silva, A. Abou-Hassan, C. Wilhelm, *ACS Nano* **2018**, *12*, 6523.

[143] S. Das, N. Debnath, S. Mitra, A. Datta, A. Goswami, *Biometals* **2012**, *25*, 1009.

[144] V. V. Elagin, E. A. Sergeeva, M. L. Bugrova, N. I. Ignatova, D. V. Yuzhakova, N. N. Denisov, V. A. Nadtochenko, E. V. Zagaynova, *Photon. Lasers Med.* **2014**, *3*, 351.

[145] S. A. Maier, *Plasmonics: Fundamentals and applications*, Springer, New York, NY **2007**.

[146] G. C. Papavassiliou, *Prog. Solid State Chem.* **1979**, *12*, 185.

[147] U. Kreibig, M. Vollmer, *Optical Properties of Metal Clusters*, Springer Science & Business Media, Berlin, Germany **2013**.

[148] T. Wriedt, Mie theory: a review. in The Mie Theory. *Springer Series in Optical Sciences. vol. 169* (Eds: W. Hergert, T. Wriedt), Springer, Berlin, Heidelberg **2012**, p. 53.

[149] C. L. Nehl, J. H. Hafner, *J. Mater. Chem.* **2008**, *18*, 2415.

[150] J. Liu, H. He, D. Xiao, S. Yin, W. Ji, S. Jiang, D. Luo, B. Wang, Y. Liu, *Dent. Mater.* **2018**, *11*, 1833.

[151] K. D. Sattler, *Handbook of Nanophysics, Nanomedicine and Nanorobotics*, Vol. 1, CRC Press, Boca Raton, FL **2011**.

[152] C. Marianecci, M. Carafa, *Pharmaceutics* **2019**, *11*, 147.

[153] M. Kim, J. H. Lee, J. M. Nam, *Adv. Sci.* **2019**, *6*, 1900471.

[154] A. L. Chen, Y. S. Hu, M. A. Jackson, A. Y. Lin, J. K. Young, R. J. Langsner, R. A. Drezek, *Nanoscale Res. Lett.* **2014**, *9*, 454.

[155] P. K. Jain, K. S. Lee, I. H. El-Sayed, M. A. El-Sayed, *J. Phys. Chem. B* **2006**, *110*, 7238.

[156] I. H. El-Sayed, X. Huang, M. A. El-Sayed, *Cancer Lett.* **2006**, *239*, 129.

[157] A. H. P. Ho, D. Kim, M. G. Somekh, *Handbook of photonics for biomedical engineering*, Springer, Berlin **2017**.

[158] X. Huang, M. A. El-Sayed, *J. Adv. Res.* **2010**, *1*, 13.

[159] R. V. Gans, *Ann. Phys.* **1915**, *352*, 270.

[160] E. M. Purcell, C. R. Pennypacker, *Astrophys. J.* **1973**, *186*, 705.

[161] S. Link, M. B. Mohamed, M. A. El-Sayed, *J. Phys. Chem. B* **1999**, *103*, 3073.

[162] L. Qiu, T. A. Larson, E. Vitkin, L. Guo, E. B. Hanlon, I. Itzkan, K. V. Sokolov, L. T. Perelman, *Biomed. Opt. Express* **2010**, *1*, 135.

[163] L. D. Landau, J. S. Bell, M. J. Kearsley, L. P. Pitaevskii, E. M. Lifshitz, J. B. Sykes, *Electrodynamics of Continuous Media*, Elsevier, Amsterdam **2013**.

[164] K. S. Lee, M. A. El-Sayed, *J. Phys. Chem. B* **2005**, *109*, 20331.

[165] E. S. Day, J. G. Morton, J. L. West, *J. Biomech. Eng.* **2009**, *131*, 074001.

[166] C. Burda, X. Chen, R. Narayanan, M. A. El-Sayed, *Chem. Rev.* **2005**, *105*, 1025.

[167] J. H. Hodak, A. Henglein, G. V. Hartland, *J. Phys. Chem. B* **2000**, *104*, 9954.

[168] X. Kang, X. Guo, W. An, X. Niu, S. Li, Z. Liu, Y. Yang, N. Wang, Q. Jiang, C. Yan, H. Wang, Q. Zhang, *Sci. Rep.* **2017**, *7*, 42069.

[169] M. A. MacKey, M. R. K. Ali, L. A. Austin, R. D. Near, M. A. El-Sayed, *J. Phys. Chem. B* **2014**, *118*, 1319.

[170] T. K. Sau, A. L. Rogach, *Complex-Shaped Metal Nanoparticles: Bottom-Up Syntheses and Applications*, Wiley, Hoboken, NJ **2012**.

[171] S. A. Briggs, K. Hattar, Evolution of Gold Nanoparticles in Radiation Environments. in *Gold Nanoparticles-Reaching New Heights* (Ed: M. Rahman), IntechOpen, Croatia **2018**.

[172] S. Link, C. Burda, B. Nikoobakht, M. A. El-Sayed, *J. Phys. Chem. B* **2000**, *104*, 6152.

[173] S. Link, M. A. Ei-Sayed, *J. Chem. Phys.* **2001**, *114*, 2362.

[174] S. S. Chang, C. W. Shih, C. D. Chen, W. C. Lai, C. R. C. Wang, *Langmuir* **1999**, *15*, 701.

[175] Y. Akiyama, T. Mori, Y. Katayama, T. Niidome, *Nanoscale Res. Lett.* **2012**, *7*, 565.

[176] C. H. Chou, C. D. Chen, C. R. C. Wang, *J. Phys. Chem. B* **2005**, *109*, 11135.

[177] K. Setoura, Y. Okada, S. Hashimoto, *Phys. Chem. Chem. Phys.* **2014**, *16*, 26938.

[178] D. Harris-Birtill, M. Singh, Y. Zhou, A. Shah, P. Ruenraroengsak, M. E. Gallina, G. B. Hanna, A. E. G. Cass, A. E. Porter, J. Bamber, D. S. Elson, *PLoS One* **2017**, *12*, e0185990.

[179] A. J. Welch, M. J. C. Van Gemert, *Optical-thermal response of laser-irradiated tissue*, Vol. 2, Springer, Berlin **2011**.

[180] V. V. Tuchin, *Static Dyn. Light Scatt. Med. Biol.* **1993**, *1884*, 234.

[181] V. V. Tuchin, *J. Biomed. Opt.* **2016**, *21*, 071114.

[182] M. Q. Brewster, Y. Yamada, *Int. J. Heat Mass Transf.* **1995**, *38*, 2569.

[183] K. Mitra, S. Kumar, *Appl. Optics* **1999**, *38*, 188.

[184] A. D. Kim, *J. Opt. Soc. Am. A* **2004**, *21*, 820.

[185] V. Tuchin, *J. Biomed. Photonics Eng.* **2016**, *2*, 030201.

[186] R. Splinter, *An Introduction to Biomedical Optics*, Wiley, Hoboken, NJ **2006**.

[187] V. V. Tuchin, *Tissue optics: Light scattering methods and instruments for medical diagnosis*, 3rd ed., SPIE Press, Bellingham, WA **2015**.

[188] S. A. Akhmanov, S. Y. Nikitin, *Physical Optics*, Clarendon Press, Oxford **1997**.

[189] M. Born, E. Wolf, *Principles of Optics, 7th (expanded) edition*, Press Syndicate of the University of Cambridge, Cambridge, UK **1999**, p. 461.

[190] M. A. Ansari, R. Massudi, M. Hejazi, *Opt. Laser Technol.* **2009**, *41*, 746.

[191] R. W. Waynant, *Lasers in Medicine*, CRC press, Boca Raton, FL **2001**.

[192] C. T. Germer, A. Roggan, J. P. Ritz, C. Isbert, D. Albrecht, G. Müller, H. J. Buhr, *Lasers Surg. Med.* **1998**, *23*, 194.

[193] V. V. Tuchin, *J. Biomed. Opt.* **2005**, *13*, 021101.

[194] V. V. Tuchin, *J. Phys. D Appl. Phys.* **2005**, *38*, 2497.

[195] S. L. Jacques, *Phys. Med. Biol.* **2013**, *58*, R37.

[196] T. C. Vogelmann, *Annu. Rev. Plant. Physiol. Plant. Mol. Biol.* **1993**, *44*, 231.

[197] J. L. Boulnois, *Lasers Med. Sci.* **1986**, *1*, 47.

[198] S. Thomsen, *Photochem. Photobiol.* **1991**, *53*, 825.

[199] H. Ye, S. De, *Burns* **2017**, *43*, 909.

[200] S. H. Diaz, G. Aguilar, E. J. Lavernia, B. J. F. Wong, *IEEE J. Sel. Top. Quantum Electron.* **2001**, *7*, 944.

[201] S. Kodera, J. Gomez-Tames, A. Hirata, H. Masuda, T. Arima, S. Watanabe, *Int. J. Environ. Res. Public Health* **2017**, *14*, 358.

[202] J. Ma, X. Yang, Y. Sun, J. Yang, *Sci. Rep.* **2019**, *9*, 1.

[203] J. Pearce, S. Thomsen, Rate Process Analysis of Thermal Damage. in *Optical-Thermal Response of Laser-Irradiated Tissue* (Eds: A. J. Welch, M. J. C. Van Gemert), Springer, Boston, MA **1995**, p. 561.

[204] M. F. Modest, *Radiative heat transfer*, 2nd ed., Academic Press, New York **2003**.

[205] W. M. Star, B. C. Wilson, A. J. Welch, M. J. C. van Gemert, *Optical-Thermal Response of Laser-Irradiated Tissue*, Vol. 6, Plenum, New York **1995**, p. 131.

[206] Z. Qin, J. C. Bischof, *Chem. Soc. Rev.* **2012**, *41*, 1191.

[207] L. A. Dombrovsky, V. Timchenko, M. Jackson, G. H. Yeoh, *Int. J. Heat Mass Transf.* **2011**, *54*, 5459.

[208] S. Soni, H. Tyagi, R. A. Taylor, A. Kumar, *Int. J. Hyperthermia* **2013**, *29*, 87.

[209] C. F. Bohren, *Absorption and scattering of light by small particles*, Wiley, Hoboken, NJ **1983**.

[210] H. H. Pennes, *J. Appl. Physiol.* **1998**, *1*, 93.

[211] L. Zhu, *Biomed. Eng. Des. Handb. Vol. I Bioeng. Fundam.* **2009**, *1*, 2.

[212] D. Yang, M. C. Converse, D. M. Mahvi, J. G. Webster, *I.E.E.E. Trans. Biomed. Eng.* **2007**, *54*, 1382.

[213] M. Aliannezhadi, M. Minbashi, V. V. Tuchin, *Quantum Electron.* **2018**, *48*, 559.

[214] J. Mesicek, K. Kuca, *Int. J. Hyperthermia* **2018**, *34*, 1255.

[215] G. M. Hale, M. R. Querry, *Appl. Optics* **1973**, *12*, 555.

[216] Saccomandi, P., Schena, E., Di Matteo, F.M., Pandolfi, M., Martino, M., Rea, R., and Silvestri, S. (**2011**) Laser Interstitial Thermotherapy for pancreatic tumor ablation: Theoretical model and experimental validation. Proceedings of the Annual International Conference of the IEEE Engineering in Medicine and Biology Society. IEEE Engineering in Medicine and Biology Society. 5585–5588.

[217] P. Saccomandi, E. Schena, M. A. Caponero, F. M. Di Matteo, M. Martino, M. Pandolfi, S. Silvestri, *I.E.E.E. Trans. Biomed. Eng.* **2012**, *59*, 2958.

[218] M. H. Niemz, J. Langer, M. H. Niemz, *Laser-tissue interactions: Fundamentals and applications*, Springer, New York, NY **2007**.

[219] M. Ghassemi, A. Shahidian, *Nano and bio heat transfer and fluid flow*, Academic Press, New York, NY **2017**.

[220] P. Saccomandi, E. Schena, S. Silvestri, *Int. J. Hyperthermia* **2013**, *29*, 609.

[221] E. Schena, D. Tosi, P. Saccomandi, E. Lewis, T. Kim, *Sensors (Switzerland).* **2016**, *16*, 1144.

[222] B. Quesson, J. A. De Zwart, C. T. W. Moonen, *J. Magn. Reson. Imaging* **2000**, *12*, 525.

[223] L. Winter, E. Oberacker, K. Paul, Y. Ji, C. Oezerdem, P. Ghadjar, A. Thieme, V. Budach, P. Wust, T. Niendorf, *Int. J. Hyperthermia* **2016**, *32*, 63.

[224] K. Le, X. Li, D. Figueroa, R. A. Towner, P. Garteiser, D. Saunders, N. Smith, H. Liu, T. Hode, R. E. Nordquist, W. R. Chen, *J. Biomed. Opt.* **2011**, *16*, 128001.

[225] M. De Landro, P. Saccomandi, M. Barberio, E. Schena, M. J. Marescaux, M. DIana, (**2019**) Hyperspectral imaging for thermal effect monitoring in in vivo liver during laser ablation. Proceedings of the 2019 41st Annual International Conference of the IEEE Engineering in Medicine and Biology Society (EMBC). IEEE; p. 1851.

[226] R. Piñol, C. D. S. Brites, N. J. Silva, L. D. Carlos, A. Millán, Nanoscale Thermometry for Hyperthermia Applications. in *Nanomaterials for Magnetic and Optical Hyperthermia Applications* (Eds: R. M. Fratila, J. M. De La Fuente), Elsevier, Amsterdam **2018**.

[227] P. Saccomandi, E. Schena, M. Diana, J. Marescaux, G. Costamagna, Thermal treatments of tumors: Principles and

methods. in *Biomedical Engineering Challenges: A Chemical Engineering Insight* (Eds: V. Piemonte, A. Basile, T. Ito, L. Marelli), Wiley, Hoboken, NJ **2018**, p. 199.

[228] A. Katzir, *Opt. Photonics News.* **1991**, *2*, 18.

[229] F. Morra, M. De Landro, S. Korganbayev, A. Wolf, A. Dostovalov, A. Cigada, P. Saccomandi, *Opt. Fiber Technol.* **2020**, *58*, 102295.

[230] S. Korganbayev, S. Asadi, A. Wolf, A. Dostovalov, M. Zalteri, E. Schena, H. Azhari, I. S. Weitz, P. Saccomandi, *Opt. Sens. Detect.* **2020**, *VI*, 19.

[231] S. B. Devarakonda, M. R. Myers, M. Lanier, C. Dumoulin, R. K. Banerjee, *Nano Lett.* **2017**, *17*, 2532.

[232] A. Skumiel, T. Hornowski, A. Józefczak, M. Koralewski, B. Leszczyński, *Appl. Therm. Eng.* **2016**, *100*, 1308.

[233] B. Anvari, M. Motamedi, J. H. Torres, S. Rastegar, E. Orihuela, *Lasers Surg. Med.* **1994**, *14*, 386.

[234] F. Manns, P. J. Milne, X. Gonzalez-Cirre, D. B. Denham, J. Parel, D. S. Robinson, *Lasers Surg. Med.* **1998**, *23*, 94.

[235] S. A. Van Nimwegen, H. F. L'eplattenier, A. I. Rem, J. J. Van Der Lugt, J. Kirpensteijn, *Phys. Med. Biol.* **2008**, *54*, 29.

[236] Mooney, R., Schena, E., Zhumkhawala, A., Aboody, K.S., and Berlin, J.M. (**2015**) Internal temperature increase during photothermal tumour ablation in mice using gold nanorods. Proceedings of the 2015 37th Annual International Conference of the IEEE Engineering in Medicine and Biology Society (EMBC), Milan, pp. 2563–2566.

[237] G. S. Terentyuk, G. N. Maslyakova, L. V. Suleymanova, N. G. Khlebtsov, B. N. Khlebtsov, G. G. Akchurin, I. L. Maksimova, V. V. Tuchin, *J. Biomed. Opt.* **2009**, *14*, 021016.

[238] P. Battalwar, J. Gokhale, U. Bansod, *Int. J. Res. Sci. Eng.* **2015**, *1*, 9.

[239] Y. Wang, K. C. L. Black, H. Luehmann, W. Li, Y. Zhang, X. Cai, D. Wan, S. Y. Liu, M. Li, P. Kim, Z. Y. Li, L. V. Wang, Y. Liu, Y. Xia, *ACS Nano* **2013**, *7*, 2068.

[240] M. Mirrahimi, Z. Abed, J. Beik, I. Shiri, A. Shiralizadeh Dezfuli, V. P. Mahabadi, S. Kamran Kamrava, H. Ghaznavi, A. Shakeri-Zadeh, *Pharmacol. Res.* **2019**, *143*, 178.

[241] P. Oh, P. Borgström, H. Witkiewicz, Y. Li, B. J. Borgström, A. Chrastina, K. Iwata, K. R. Zinn, R. Baldwin, J. E. Testa, J. E. Schnitzer, *Nat. Biotechnol.* **2007**, *25*, 327.

[242] V. Rieke, K. B. Pauly, *J. Magn. Reson. Imaging* **2008**, *27*, 376.

[243] N. McDannold, C. M. Tempany, F. M. Fennessy, M. J. So, F. J. Rybicki, E. A. Stewart, F. A. Jolesz, K. Hynynen, *Radiology* **2006**, *240*, 263.

[244] A. Farashahi, A. Zare-Sadeghi, A. Shakeri-Zadeh, S. Kamran Kamrava, S. Maleki, H. Ghaznavi, F. Faeghi, *Photodiagn. Photodyn. Ther.* **2019**, *25*, 66.

[245] M. Zabanran, M. Asadi, A. Zare-Sadeghi, A. A. Ardakani, A. Shakeri-Zadeh, A. Komeili, S. K. Kamrava, B. Ghalandari, *Optik (Stuttg).* **2019**, 163718.

[246] M. A. Lewis, R. M. Staruch, R. Chopra, *Int. J. Hyperthermia* **2015**, *31*, 163.

[247] R. M. Lemor, B. V. Kleffner, S. Tretbar, R. M. Schmitt, Ultrasound temperature and attenuation monitoring for controlling the laser induced thermo therapy. in *Acoustical Imaging* (Eds: M. P. André, I. Akiyama, M. Andre, W. Arnold, J. Bamber, V. Burov, N. Chubachi, K. Erikson, H. Ermert, M. Fink, W. S. Gan, B. Granz, J. Greenleaf, J. Hu, J. P. Jones, P. Khuri-Yakub, P. Laugier, H. Lee, S. Lees, V. M. Levin, R.

Maev, L. Masotti, A. Nowicki, W. O'Brien, M. Prasad, P. Rafter, D. Rouseff, J. Thijssen, B. Tittmann, P. Tortoli, A. Van der Steen, R. Waag, P. Wells), Springer, Dordrecht **2002**, p. 395.

[248] L. E. Cole, R. D. Ross, J. M. Tilley, T. Vargo-Gogola, R. K. Roeder, *Nanomedicine* **2015**, *10*, 321.

[249] M. M. Mahan, A. L. Doiron, *J. Nanomater* **2018**, *2018*, 5837276.

[250] M. Şologan, F. Padelli, I. Giachetti, D. Aquino, M. Boccalon, G. Adami, P. Pengo, L. Pasquato, *Nanomaterials* **2019**, *9*, 879.

[251] O. Perlman, I. S. Weitz, H. Azhari, *Int. J. Hyperthermia* **2018**, *34*, 773.

[252] P. Homolka, A. Gahleitner, R. Nowotny, *Phys. Med. Biol.* **2002**, *47*, 2917.

[253] P. Bruners, G. D. Pandeya, E. Levit, E. Roesch, T. Penzkofer, P. Isfort, B. Schmidt, M. J. W. Greuter, M. Oudkerk, T. Schmitz-Rode, C. K. Kuhl, A. H. Mahnken, *Int. J. Hyperthermia* **2012**, *28*, 55.

[254] G. D. Pandeya, J. H. G. M. Klaessens, M. J. W. Greuter, B. Schmidt, T. Flohr, R. Van Hillegersberg, M. Oudkerk, *Eur. Radiol.* **2011**, *21*, 1733.

[255] F. Fani, E. Schena, P. Saccomandi, S. Silvestri, *Int. J. Hyperthermia* **2014**, *30*, 219.

[256] M. Pramanik, L. V. Wang, *J. Biomed. Opt.* **2009**, *14*, 054024.

[257] J. Shah, S. Park, S. Aglyamov, T. Larson, L. Ma, K. Sokolov, K. Johnston, T. Milner, S. Y. Emelianov, *J. Biomed. Opt.* **2008**, *13*, 034024.

[258] T. T. V. Phan, N. Q. Bui, S. W. Cho, S. Bharathiraja, P. Manivasagan, M. S. Moorthy, S. Mondal, C. S. Kim, J. Oh, *Sci. Rep.* **2018**, *8*.

[259] S. Wang, Z. Dai, H. Ke, E. Qu, X. Qi, K. Zhang, J. Wang, *Eur. J. Radiol.* **2014**, *83*, 117.

[260] H. Ke, J. Wang, Z. Dai, Y. Jin, E. Qu, Z. Xing, C. Guo, X. Yue, J. Liu, *Angew. Chem. Int. Ed.* **2011**, *50*, 3017.

[261] T. Curry, R. Kopelman, M. Shilo, R. Popovtzer, *Contrast Media Mol. Imaging* **2014**, *9*, 53.

[262] Y.-H. Wang, A.-H. Liao, J.-H. Chen, C.-R. Chris Wang, P.-C. Li, *J. Biomed. Opt.* **2012**, *17*, 045001.

[263] S. Rajkumar, M. Prabaharan, *Curr. Top. Med. Chem.* **2017**, *17*, 1858.

[264] W. Li, X. Chen, *Nanomedicine* **2015**, *10*, 299.

[265] R. Cheheltani, R. M. Ezzibdeh, P. Chhour, K. Pulaparthi, J. Kim, M. Jurcova, J. C. Hsu, C. Blundell, H. I. Litt, V. A. Ferrari, H. R. Allcock, C. M. Sehgal, D. P. Cormode, *Biomaterials* **2016**, *102*, 87.

[266] M. M. Paulides, P. R. Stauffer, E. Neufeld, P. F. MacCarini, A. Kyriakou, R. A. M. Canters, C. J. Diederich, J. F. Bakker, G. C. Van Rhoon, *Int. J. Hyperthermia* **2013**, *29*, 346.

[267] Z. Rijnen, J. F. Bakker, R. A. M. Canters, P. Togni, G. M. Verduijn, P. C. Levendag, G. C. Van Rhoon, M. M. Paulides, *Int. J. Hyperthermia* **2013**, *29*, 181.

[268] J. W. Hand, *Phys. Med. Biol.* **2008**, *53*, R243.

[269] P. Deuflhard, A. Schiela, M. Weiser, *Acta Numer.* **2012**.

[270] G. Yona, N. Meitav, I. Kahn, S. Shoham, *eNeuro.* **2016**, *3*.

[271] S. Soni, H. Tyagi, R. A. Taylor, A. Kumar, *J. Therm. Biol.* **2014**, *43*, 70.

[272] F. Rossi, F. Ratto, R. Pini Laser activated gold nanorods for the photothermal treatment of cancer. Excerpt from the Proceedings of the 2012 COMSOL Conference in Milan. **2012**.

[273] Y. Xu, S. Long, Y. Yang, F. Zhou, N. Dong, K. Yan, B. Wang, Y. Zeng, N. Du, X. Li, W. R. Chen, *Theor. Biol. Med. Model.* **2019**, *16*, 12.

[274] E. Oakley, B. Wrazen, D. A. Bellnier, Y. Syed, H. Arshad, G. Shafirstein, *Lasers Surg. Med.* **2015**, *47*, 60.

[275] G. Shafirstein, D. A. Bellnier, E. Oakley, S. Hamilton, M. Habitzruther, L. Tworek, A. Hutson, J. A. Spernyak, S. Sexton, L. Curtin, S. G. Turowski, H. Arshad, B. Henderson, *Br. J. Cancer* **2018**, *119*, 1191.

[276] B. Gheflati, N. Naghavi. Optimization of laser power for laser-induced hyperthermia in the presence of nanoparticles using MATLAB and COMSOL multiphysics. 2019 27th Iranian Conference on Electrical Engineering (ICEE), Yazd, Iran, pp. 1787–1792. **2019**.

[277] K. Shurrab, N. Kochaji, W. Bachir, *J. Lasers Med. Sci.* **2017**, *8*, 118.

[278] OpenGATE Collaboration. Forewords GATE. **2015**. Available from http://www.opengatecollaboration.org/.

[279] V. Cuplov, I. Buvat, F. Pain, S. Jan, *J. Biomed. Opt.* **2014**, *19*, 026004.

[280] S. Jan, G. Santin, D. Strul, S. Staelens, K. Assié, D. Autret, S. Avner, R. Barbier, M. Bardiès, P. M. Bloomfield, D. Brasse, V. Breton, P. Bruyndonckx, I. Buvat, A. F. Chatziioannou, Y. Choi, Y. H. Chung, C. Comtat, D. Donnarieix, L. Ferrer, S. J. Glick, C. J. Groiselle, D. Guez, P. F. Honore, S. Kerhoas-Cavata, A. S. Kirov, V. Kohli, M. Koole, M. Krieguer, D. J. van der Laan, F. Lamare, G. Largeron, C. Lartizien, D. Lazaro, M. C. Maas, L. Maigne, F. Mayet, F. Melot, C. Merheb, E. Pennacchio, J. Perez, U. Pietrzyk, F. R. Rannou, M. Rey, D. R. Schaart, C. R. Schmidtlein, L. Simon, T. Y. Song, J. M. Vieira, D. Visvikis, R. Van de Walle, E. Wieërs, C. Morel, *Phys. Med. Biol.* **2004**, *49*, 4543.

[281] S. Jan, D. Benoit, E. Becheva, T. Carlier, F. Cassol, P. Descourt, T. Frisson, L. Grevillot, L. Guigues, L. Maigne, C. Morel, Y. Perrot, N. Rehfeld, D. Sarrut, D. R. Schaart, S. Stute, U. Pietrzyk, D. Visvikis, N. Zahra, I. Buvat, *Phys. Med. Biol.* **2011**, *56*, 881.

[282] V. Cuplov, F. Pain, S. Jan, *Biomed. Opt. Express* **2017**, *8*, 1665.

[283] W. Lu, C. Xiong, G. Zhang, Q. Huang, R. Zhang, J. Z. Zhang, C. Li, *Clin. Cancer Res.* **2009**, *15*, 876.

[284] A. M. Gamal-Eldeen, D. Moustafa, S. M. El-Daly, M. A. M. Abo-Zeid, S. Saleh, M. Khoobchandani, K. Katti, R. Shukla, K. V. Katti, *Biomed. Pharmacother.* **2017**, *89*, 1045.

[285] S. K. Cho, K. Emoto, L. J. Su, X. Yang, T. W. Flaig, W. Park, *J. Biomed. Nanotechnol.* **2014**, *10*, 1267.

[286] T. S. Hauck, T. L. Jennings, T. Yatsenko, J. C. Kumaradas, W. C. W. Chan, *Adv. Mater.* **2008**, *20*, 3832.

[287] W. Zhou, X. Liu, J. Ji, *J. Nanopart. Res.* **2012**, *14*.

[288] C. Ash, M. Dubec, K. Donne, T. Bashford, *Lasers Med. Sci.* **2017**, *32*, 1909.

[289] E. Hutter, J. H. Fendler, *Adv. Mater.* **2004**, *16*, 1685.

[290] J. H. Bin, P. V. Tsalu, J. W. Ha, *Sci. Rep.* **2019**, *9*.

[291] M. Shabaninezhad, G. Ramakrishna, *J. Chem. Phys.* **2019**, *150*.

[292] M. Liu, P. Guyot-Sionnest, *J. Phys. Chem. B* **2005**, *109*, 22192.

[293] T. R. Jensen, M. L. Duval, K. Lance Kelly, A. A. Lazarides, G. C. Schatz, R. P. Van Duyne, *J. Phys. Chem. B* **1999**, *103*, 9846.

APPENDIX

Gans theory or Mie-Gans theory is the extension of Mie theory. It is the solution of Maxwell equations to characterize the scattering for the prolate or oblate spheroid shape particles smaller than the excitation wavelength. In this theory, the absorption only depends on the AR (ie, the ratio of particle size in different dimensions) and is not dependent on the absolute dimension. This dependency is determined by the defined factors that are related to the shape of particles in three dimensions. In fact, the Gans theory was developed to explain the optical properties of ellipsoid shaped particles based on the dipole approximation.

The Mie solution to Maxwell's equations describes the scattering and absorption of incident light by spherical particles, based on the relationship for the extinction cross-section, C_{ext} ($C_{ext} = C_{abs} + C_{sca}$), that is, the sum of the absorption cross-section and the scattering cross-section of the metal nanoparticles. For small particles ($d \ll \lambda$), the Mie solution is represented by:

$$C_{ext} = 9 \frac{\omega}{c} \varepsilon^{\frac{3}{2}} V_0 \frac{\varepsilon_2(\omega)}{[\varepsilon_r(\omega) + 2\varepsilon_m]^2 + \varepsilon_i(\omega)^2} \quad (A1)$$

where $V_0 = \frac{4\pi}{3} R^3$ is the volume of particle, ω is the angular frequency of the extinction radiation, ε is the complex dielectric constant of the metal given by $\varepsilon = \varepsilon_r(\omega) + i\varepsilon_i(\omega)$, while $\varepsilon_r(\omega)$ is the real part and $\varepsilon_i(\omega)$ is the imaginary part of dielectric constant of the metal, respectively. ε_m is the real part of the dielectric constant of the surrounding medium. The surface plasmon absorption band appears when $\varepsilon_r(\omega) \approx -2\varepsilon_m$ if $\varepsilon_i(\omega)$ is small or if it is only weakly dependent on ω. The bandwidth and amplitude of the peak are well approximated by $\varepsilon_i(\omega)$; however, the size dependency of the position of the surface plasmon absorption band of the metal NPs can be adapted by assuming size-dependent dielectric functions [289].

For more sensitive detection of the LSPR signal, NP shape is an important factor. This characteristic is well described and showed how it is affected by the nanoparticle shape and size, and that more detailed properties can be found in more complicated geometries [149, 290, 291].

The NRs are formed by asymmetric growth of small gold spheres in the presence of shape-forming surfactants, weak reducing agents, and the catalysts [292]. According to Gans theory, the extinction coefficient σ can be quantitatively expressed as [161]:

$$\sigma = \frac{2\pi N V \varepsilon_m^{3/2}}{3\lambda} \sum_j \frac{\left(\frac{1}{P_j^2}\right) \varepsilon_2}{\left(\varepsilon_1 + \frac{1-P_j}{P_j} \varepsilon_m\right)^2 + \varepsilon_2^2} \quad (A2)$$

where N is the number of NPs per unit of volume, V is the volume of each NP, λ is the wavelength of the incident light, P_j is defined as

$$P_A = \frac{1-e^2}{e^2} \left[\frac{1}{2e} \ln\left(\frac{1+e}{1-e}\right) - 1\right] \quad e = \sqrt{1 - \left(\frac{B}{A}\right)^2} \quad (A3)$$

$$P_B = P_C = \frac{1-P_A}{2} \quad (A4)$$

where j represents the three dimensions of the particle, A, B, and C are the three axes of the rods and P_j termed depolarization factors for each axis of the prolate B is the AR/B is the AR. The resonance occurs at $\varepsilon_1 = -\frac{(1-p_j^{(i)}) \, \varepsilon m}{p_j^{(i)}}$ where $i = A$ for longitudinal resonance and $i = B,C$ for transverse resonance. The wavelength of the LSPR peak is dependent on the dielectric function of the surrounding medium [293]. This phenomenon can be demonstrated by the Drude model, represented as:

$$\varepsilon_r = 1 - \frac{w_p^2}{w^2 + \gamma^2} \quad (A5)$$

where w_p is the plasmon frequency and γ is the damping factor of the bulk metal. In the visible and NIR regions, in the case of $\gamma \ll w_p$, we can simplify this equation to

$$\varepsilon_r = 1 - \left(\frac{w_p}{w}\right)^2 \quad (A6)$$

that under resonance condition ($\varepsilon_r = -2\varepsilon_m$), then we have.

$$W_{max} = \frac{w_p}{\sqrt{2\varepsilon_m + 1}} \quad (A7)$$

where W_{max} is the frequency of the LSPR peak.

If the frequency is substituted by the wavelength via $\lambda = 2\pi c/\omega$, and then the dielectric constant is replaced by refractive index via $\varepsilon_m = n^2$, we will have

$$\lambda_{max} = \lambda_p \sqrt{2n_m^2 + 1} \quad (A8)$$

where λ_{max} is the wavelength at the LSPR peak and λ_p is the wavelength corresponding to the plasma frequency of the bulk metal. From a general point of view, in presence

of GNPs under laser light, the temperature increase is given by the heat contributed by a large number (N) of GNPs, each particle generating a certain amount of heat (Q_{nps}), which is given by the product of absorption cross-section area (C_{abs}) and laser fluence (I) $= C_{abs} \cdot I$). The resulting Specific Absorption Rate (SAR) for N particles is, therefore, given by Equation (9)

$$SAR = N \cdot Q_{NPs} = N \cdot C_{abs} \cdot I = \mu_{a,NPs} \cdot I \qquad (A9)$$

where $N \cdot C_{abs}$ defines the absorption coefficient $\mu_{a,NPs}$ of the particles. GNPs with high scattering increase the internal diffuse radiation, whereas GNPs with high absorption produce a large amount of SAR at the entry region, that is, the region near the laser source. For all the light transport modeling methods mentioned above, the optical properties of the NP laden tissue are fundamental inputs and need to be described accurately.